ACS Catalysis

Review

pubs.acs.org/acscatalysis

Heteroatom-Doped Graphene-Based Materials for Energy-Relevant Electrocatalytic Processes

Jingjing Duan,[†] Sheng Chen,[†] Mietek Jaroniec,[‡] and Shi Zhang Qiao*[,†]

[†]School of Chemical Engineering, The University of Adelaide, Adelaide, South Australia 5005, Australia

[‡]Department of Chemistry and Biochemistry, Kent State University, Kent, Ohio 44240, United States

ABSTRACT: To address aggravating energy and environment issues, inexpensive, highly active, and durable electrocatalysts as noble metal substitutes both at the anode and cathode are being actively pursued. Among them, heteroatom-doped graphene-based materials show extraordinary electrocatalytic performance, some even close to or outperforming the state-of-the-art noble metals, such as Pt- and IrO_2-based materials. This review provides a concise appraisal on graphene doping methods, possible doping configurations and their unique electrochemical properties, including single and double doping with N, B, S, and P. In addition, heteroatom-doped graphene-based materials are reviewed as electrocatalysts for oxygen reduction, hydrogen evolution, and oxygen evolution reactions in terms of their electrocatalytic mechanisms and performance. Significantly, three-dimensional heteroatom-doped graphene structures have been discussed, and those especially can be directly utilized as catalyst electrodes without extra binders and supports.

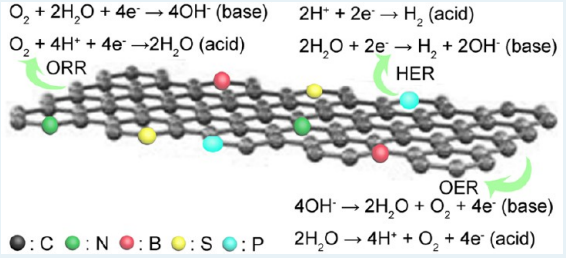

KEYWORDS: *heteroatom-doped graphene, nonnoble electrocatalysts, oxygen reduction reaction, hydrogen evolution reaction, oxygen evolution reaction*

1. INTRODUCTION

1.1. Graphene-Based Materials for Electrocatalysis.

Electrocatalysis, which was first introduced by Kobosev and Monblanowa in 1936,[1,2] can be explained as the acceleration of an electrochemical process occurring on the electrode surface. Heterogeneous electrocatalytic reactions generally involve interactions of the reactants, intermediates, or products with the electrode surface. Consequently, the electrocatalytic performance is highly dependent on the electrode material, specifically its surface area, electroconductivity, catalytic activity, long-term stability, etc.[3]

Since 2004 when graphene was first prepared via the "Scotch tape" method, it has emerged as the subject of intense research, especially as the key component of electrode materials.[4] Graphene is an indefinitely extended two-dimensional (2D) carbon crystal, in which carbon atoms are packed in a hexagonal lattice resembling a honeycomb.[4,5] Significantly, numerous fascinating properties of graphene have been reported, including high specific surface area, excellent mechanical strength and flexibility, and unparalleled thermal and electrical conductivity as well as superior electronic properties. Numerous methods have been developed to synthesize graphene, such as the Hummers method, chemical vapor deposition (CVD), direct liquid exfoliation, etc.[6−9] Meanwhile, the raw materials used to prepare graphene, such as natural graphite, carbons, polymers, biomass wastes, etc., are abundant.[10,11] The availability of effective methods of synthesis and a large variety of precursors as well as the unique properties of graphene make it a very promising candidate for large-scale production and commercialization of energy devices.

From the condensed matter viewpoint, graphene is constructed of sp^2-bonded carbon atoms via hybridization of s, p_x, and p_y atomic orbitals, forming three strong σ bonds with three adjacent atoms. The remaining p_z orbital on each carbon overlaps with those from neighboring atoms, establishing a filled band of π orbitals (valence band) and an empty band of π^* orbitals (conduction band). Therefore, graphene can be considered either as a metal with vanishing Fermi surface or a semiconductor with zero bandgap. The lack of intrinsic bandgap greatly limits the applications of pristine graphene in such areas as nanoelectronics, energy storage and electrocatalysis, so it is appealing to induce a bandgap in graphene to advance the aforementioned applications.[12−14] Several methods have been proposed to open the bandgap in graphene, such as chemical functionalization, multilayer graphene, molecular adsorption, confinement, and edge-effects-induced bandgap.[15−18] For example, new electronic properties arise when various morphologies of graphene are obtained, including zero-dimensional (0D) graphene quantum dots (GQDs) and one-dimensional (1D) graphene nanoribbons (GNRs), which are highly dependent on the size and edge lattice symmetry.[18,19] The predominantly zigzag-edged, 2.3 nm-wide GNRs exhibit a smaller bandgap (0.14 eV) than the 2.9-nm-wide armchair GNRs (0.38 eV), suggesting that the higher concentration of zigzag edges tends to decrease the energy gap as a result of the

Received: May 12, 2015
Revised: July 9, 2015
Published: July 23, 2015

DOI: 10.1021/acscatal.5b00991
ACS Catal. 2015, 5, 5207−5234

staggered sublattice potential along the zigzag-terminated edges.

Other than morphology control, chemical doping with foreign atoms is also an effective method to tailor electronic properties, manipulate surface chemistry, and modify the elemental composition of host materials.[20−23] Generally, there are two types of chemically doped graphene.[24] In the first type, known as surface transfer doping, the agents adsorb onto the surface of graphene and do not cause sp^3 defects in graphene lattice. In the second type, known as the substitutional doping, the agents can disrupt the sp^2 network and cause sp^3 defect regions via covalent bonding with graphene. In this review, we focus on the substitutional heteroatom-doping of graphene, in which carbon atoms in graphene lattice are substituted by single/multiple nitrogen (N), boron (B), sulfur (S) and phosphorus (P) atoms.

In recent years, the heteroatom-doped graphene has been extensively investigated in the field of electrocatalysis.[22,25−28] As compared with the previously reported reviews, this paper not only elaborates the doping methods but also addresses the unique electrochemical properties of different doping configurations for each doping type (N/B/S/P). Moreover, the role of heteroatom-doped graphene in the hybrid electrocatalysts has been discussed in relation to the conductivity and active sites for electrocatalysis. Importantly, the strong coupling between doped graphene and metal centers not only facilitates the electron transfer between them, which results in the enhancement of the electroactivity, but also improves the working durability because of the covalent bonding between metal and dopants. Significantly, macroscopic three-dimensional (3D) graphene structures are exclusively reviewed, especially those that can be directly utilized as catalyst electrodes without extra binders and supports. We conclude this paper with some perspectives on the future developments in this intriguing field; for instance, the controllability of doping configurations, ambiguous doping mechanism, and large-scale production of heteroatom-doped graphene materials for commercialization.[29]

1.2. Oxygen Reduction Reaction (ORR). Instead of burning fuels to create heat, fuel cells (FCs) convert chemical energy directly into electricity.[30] In FCs, H_2(gas) at the anode splits into electrons and protons via the hydrogen oxidation reaction (HOR): the protons diffuse to the cathode through the cell while the electrons flow out of the anode to provide electricity. On the other hand, O_2(gas) at the cathode reacts with electrons and protons to form water, which is known as ORR. It has been reported that more than half of the cost in the polymer electrolyte membrane FCs (PEMFCs) refers to the Pt-based catalyst that is used to facilitate HOR and ORR.[31] The anodic HOR is quite facile, so it requires only a small amount of Pt; in contrast, the kinetics of the cathodic ORR is sluggish and requires a large amount of Pt catalyst. Nevertheless, the high cost, low tolerance to methanol/CO, limited durability, and insufficient activity of exclusively used Pt catalysts for ORR greatly hamper the commercial development of FCs.

Generally, the efforts to reduce the cost of FCs include two approaches. The first strategy is to reduce Pt usage by alloying Pt with inexpensive metals (Fe, Ni, etc.)[32,33] or depositing Pt on porous and conductive supports such as carbon.[34,35] Although the required Pt loading has been reduced significantly in the past decade, the increasing price of Pt has greatly compromised the Pt loading reduction, making this approach effective only for the short term. The other approach is to develop nonprecious metal-based electrocatalysts with activity comparable to that of Pt that feature good tolerance to methanol/CO and a long lifespan; this approach can be considered a long-term and sustainable solution. For a practical nonprecious catalyst used in PEMFCs, the Department of Energy of the United States has set up activity and stability 2020 targets: the ORR activity must reach a volumetric current density of 300 A cm^{-3} at 0.8 $V_{iR\text{-free}}$, and the stability must reach 5000 h at operating temperatures below 80 °C.[36]

1.3. Hydrogen Evolution Reaction (HER). To address the sustainability, environmental emissions, and security issues of the current energy systems, H_2 is considered as the future energy carrier to replace the finite fossil fuels.[37,38] The hydrogen economy was first recognized in 1874 by Jules Verne, and since then, H_2 has become popular as a new-generation transportation fuel and energy storage medium.[37] Generally speaking, H_2 can be generated using coal gasification, natural gas, biomass, or water. Although coal gasification could produce large amounts of H_2 economically, its finite resource and greenhouse gas emission make this approach unsustainable.[39] Currently, natural gas is widely used to produce H_2 to provide an initial foray into the hydrogen economy, but it is still problematic because of the increasing depletion rate of fossil fuels and environmental emissions.[40] On the other hand, although the biomass approach is clean and sustainable, it cannot supply a sufficient amount of H_2.[41] Among the four aforementioned resources, water is the only sustainable and clean resource to produce hydrogen in the future because it is almost inexhaustible on the earth. Nevertheless, the direct thermal splitting of water requires very high temperatures (~2000 °C) and the generated H_2 and O_2 recombine rapidly.

Promoted by effective electrocatalysts, H_2 can be separately produced through cathodic HER in electrocatalytic water splitting at ambient conditions, driven by small overpotentials.[2,42] The state-of-the-art Pt-based electrocatalysts for HER exhibit high activity, but their high cost and limited durability greatly limits their commercialization.[38,43] As a consequence, highly efficient, inexpensive and durable electrocatalysts for HER to substitute Pt are highly desirable. Recently, tremendous efforts have been made in this direction, For example, transition metals of Co, Ni, Fe, Mo, and W and their sulfides, phosphides, carbides, nitrides, and molecular derivatives have been explored despite their corrosion susceptibility to acidic/basic electrolytes.[44−48] In addition, the membrane electrode assembly process, which involves the dissolution of a catalyst powder with binders in solvents, casting the resulting ink on supports such as copper foil and glassy carbon followed by drying, would compromise the catalyst performance because of the unavoidable catalyst agglomeration and peeling off during gas-involving processes such as HER.[49,50] Therefore, not only the catalyst morphology, size, and chemical composition but also the electrode architecture are highly important in practical HER applications.

1.4. Oxygen Evolution Reaction (OER). Conversion of renewable energy (solar, wind, and geothermal) into chemical fuels, such as molecular hydrogen and hydrocarbons (methanol, methane, formic acid, etc.), provides a promising pathway for large-scale energy storage.[30,51−54] The state-of-the-art method for hydrogen generation is water splitting[52] and for hydrocarbon generation is carbon dioxide reduction.[54] The essential counterpart reaction for these reactions is OER, which involves the generation of oxygen molecules at the anode. Meanwhile, OER is also a very important reaction in many other energy-

DOI: 10.1021/acscatal.5b00991
ACS Catal. 2015, 5, 5207−5234

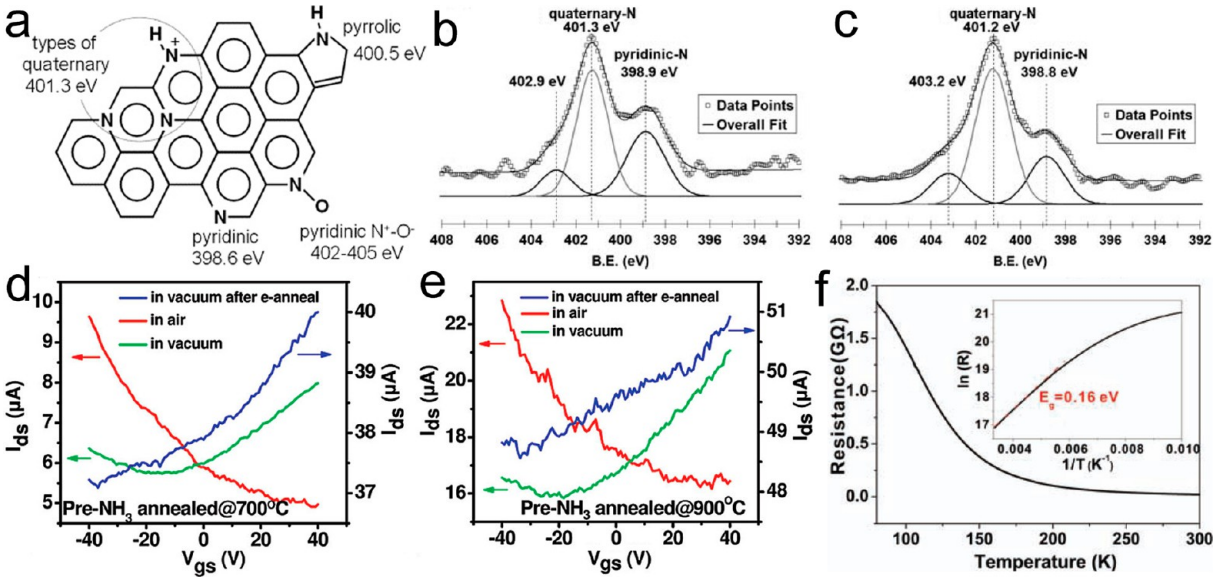

Figure 1. (a) N-Doping configurations in NG. (b,c) Comparison of the XPS spectra of the N 1s region for Vulcan carbon treated for 2 h at 900 °C with acetonitrile. The sample in part b was exposed to the atmosphere; the sample in part c was transferred to XPS via a controlled atmosphere transfer chamber. Reproduced with permission from Ozkan et al.[80] Copyright 2006, Elsevier. (d) Current-gate voltage (I_{ds}−V_{gs}) curves (recorded at V_{ds} = 1 V) of a single GO device fabricated with an NH_3-annealed (700 °C) GO sheet. Red solid line: device tested in air. Green solid line: device tested in vacuum. Blue solid line: device tested in vacuum after electrical annealing. (e) Current-gate voltage (I_{ds}−V_{gs}) curves of a single GO device fabricated with an NH_3-annealed (900 °C) GO sheet. Red solid line: device tested in air. Green solid line: device tested in vacuum. Blue solid line: device tested in vacuum after electrical annealing. Reproduced with permission from Dai et al.[87] Copyright 2009, American Chemical Society. (f) Temperature dependence of the electrical resistance (R) of NG (N/C = 2.9 at. %). The inset shows the change of ln(R) as a function of T^{-1} in the temperature range from 100 to 300 K. Reproduced with permission from Liu et al.[89] Copyright 2011, Wiley VCH.

Table 1. Summary of Nitrogen-Doped Graphene and Its Applications

method	precursors	doping structure	doping level	applications, refs
thermal annealing	GO, NH_3	pyridinic, pyrrolic, graphitic N	5%	87
	Ni(C)/B(N)/SiO_2/Si substrate	pyridinic, pyrrolic, graphitic N	0.3−2.9 N/C at. %	89
	3D NGF: GO, 5 vol % pyrrole	pyridinic, pyrrolic N	4.2 at. %	ORR[91]
	sugar, urea	pyridinic, pyrrolic, graphitic N, N oxide	3.02−11.2 at. %	ORR[92]
	GO, copper amine complex	pyridinic, pyrrolic, graphitic N, N oxide	2.85−2.45 at. %	ORR[180]
CVD	pyridine	pyridinic, graphitic N	2.4 at. %	85
	H_2, C_2H_4, NH_3 on Cu foils	pure pyridinic N	16 at. %	ORR[93]
	CH_4, NH_3 on Cu foils	pyridinic, pyrrolic, graphitic N	8.9 at. %	94
	triazine on a Ni(111) film	pyridinic, 80% graphitic N	1−2 at. %	96
	CH_4, H_2, NH_3 on Cu foils	graphitic N	0.23−035 N/C at. %	95
	pyridine		16.7 at. %	98
solvothermal synthesis	GO, N_2H_4, NH_3	pyridinic, pyrrolic, graphitic, pyridinic N oxides	5 wt %	99
	GO, urea	pyridinic, pyrrolic, graphitic N	10.13 at. %	capacitive behaviors[84]
	CCl_4, LiN	pyridinic, pyrrolic, graphitic N	16.4% N/C	82
supercritical reaction	graphite, acetonitrile	pyridinic, pyrrolic, graphitic N	1.57−4.56 at. %	100
arc discharge	graphite, pyridine/ammonia	pyridinic, graphitic N	0.6−1.4 at. %	88
plasma	graphene, nitrogen plasma	pyridinic, pyrrolic, graphitic, pyridinic N oxides	8.5 at. %	ORR, H_2O_2 reduction[90]
nitrogen bombardment	graphene on Ni(111)	pyridinic, graphitic N		101
ball-milling	graphite in N_2	pyridinic, pyrrolic N	14.84 wt %	solar cells, ORR[102]

related devices, such as reversible fuel cells, metal−air batteries, and solar cells.[30,51,53] OER is known to have an intrinsically very sluggish reaction kinetics caused by the multiple proton-couple electron-transfer steps, requiring the use of an effective electrocatalyst for enhancing the reaction rate.[55−58] The most efficient catalysts for OER are noble metal oxides, such as Ir- and Ru-based materials.[59−65] To replace expensive Ir and Ru, numerous efforts have been undertaken toward using transition metal alternatives (Co, Fe, Mn, Ni, etc.), in which metal species are considered the active sites.[57,66−68] Recently, a few nonmetal materials, including heteroatom-doped graphene, have been reported as a new category of OER electrocatalysts.[56,69−72] Other than heterogeneous catalysts, homogeneous catalysts have also attracted enormous interest as electrocatalysts for OER (Ru, Co, Cu, Fe, etc.) because of their highly active centers and the simplicity of methods for studying OER mechanism.[58,73−78]

2. HETEROATOM-DOPED GRAPHENE

2.1. N-doped Graphene (NG). *2.1.1. N-Doping Configurations.* The larger electronegativity of N (3.04) than that of

DOI: 10.1021/acscatal.5b00991
ACS Catal. 2015, 5, 5207−5234

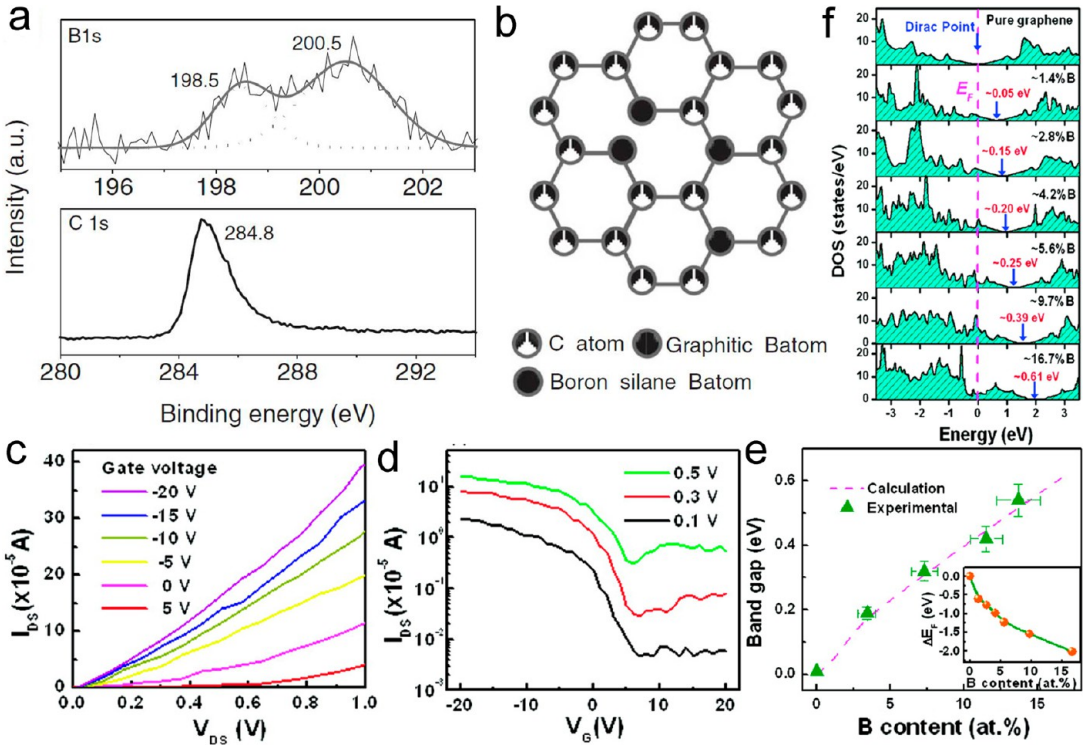

Figure 2. (a) XPS spectra of B 1s and C 1s in BG. (b) B-doping configuration. Reproduced with permission from Zhu et al.,[105] Copyright 2012, Wiley VCH. (c) $I_{ds}-V_{gs}$ plots of a typical field-effect transistor (FET) made of BG obtained by microwave plasma in a boron ion atmosphere. (d) $I_{ds}-V_{gs}$ plots at V_{DS} = 0.1, 0.3, and 0.5 V. (e) Experimental band gaps and the corresponding calculation results of BG vs B content for various FETs. Inset: dependence of doping level (the position of the Fermi level from the Dirac point) on the B content. (f) Calculated DOS in BG with different B contents. The Fermi level is labeled by the red dashed line. Reproduced with permission from Lee et al.[103] Copyright 2012, American Chemical Society.

C (2.55) creates polarization in the carbon network, thereby influencing the electronic, magnetic, and optical properties of graphene.[79] Generally, there are three bonding configurations of N in graphene matrix, including pyridinic, pyrrolic, and graphitic N (also known as quaternary N), which exhibit different binding energies (BE) in X-ray photoelectron spectroscopy (XPS) spectra (Figure 1a–c).[80−83] Pyridinic N (sp^2 hybridized) is bonded to two C atoms at graphene edges and contributes one p electron to the π system; pyrrolic N (sp^3 hybridized) contributes two p electrons to the π system into a five-membered ring; graphitic N, being also sp^2 hybridized, substitutes C atoms in hexagonal rings. In addition, N oxides of pyridinic N in which one N atom is bonded with two C atoms and one O atom are observed. Different configurations are possible and may be advantageous for various practical applications.[84,85] For example, because of the similar C−N (1.41 Å) and C−C (1.42 Å) bond lengths, pyridinic and graphitic N atoms exert a marginal influence on the graphene structure. Sun et al. indicated that pyridinic N and pyrrolic N in NG are essential for improving pseudocapacitance by taking advantage of redox reactions, whereas graphitic N could enhance conductivity, which favors electron transport during charge/discharge process.

2.1.2. N-Doping Effect. N-Doping can induce a bandgap near the Dirac point by suppressing the nearby density of states (DOS), thereby endowing graphene with n-type semiconducting properties.[86−89] As shown in Figure 1d–e, graphene oxide (GO) annealed in air exhibits p-type behavior because of the physisorbed oxygen, whereas the Dirac point of GO annealed with NH_3 in vacuum is at negative gate voltages (V_{gs} < ∼−20), indicating n-type behavior. The NH_3-annealed GO subjected to further removal of physisorbed species exhibits fully n-type behavior, with the Dirac point at highly negative gate voltages.[87] In addition, it was shown that the n-type behavior of NG can be systematically tuned by adjusting the N-doping level.[88] A bandgap of 0.16 eV reported for NG by Zhang et al. suggests that N-doping can be used to tune the electrical properties of graphene (Figure 1f).[89] Significantly, Shao et al. reported that the presence of N enhances the ability of graphene to donate electrons to the adjacent carbon atoms, which is advantageous for such reactions as ORR and H_2O_2 reduction.[90]

2.1.3. Appraisal of Methods for Synthesis of NG. Table 1 summarizes the main methods for synthesis of NG. In 2009, Hongjie Dai's group reported a high-power electrical joule heating method to N-dope GNRs using NH_3, which was shown to occur mostly at the edges of GNRs because of their high chemical reactivity.[86] Shortly after, they developed a thermal annealing method for the preparation of NG using GO and NH_3, which was later widely explored by using different N precursors, including gases, solids, etc.[87,91,92] The XPS study showed that the N-doping can be tuned by adjusting the doping temperatures, and the doping level can be enlarged by increasing the concentration of oxygen groups at the defect and edge sites of GO. Significantly, Qu's group reported a 3D NG foam fabricated from pyrrole, which features high surface area, light weight, well-developed porosity, mechanical stability, and electrical conductivity, thus offering great technological potential for a variety of applications, such as energy storage, adsorption, and electrocatalysis.[91]

DOI: 10.1021/acscatal.5b00991
ACS Catal. 2015, 5, 5207−5234

Table 2. Summary of Boron-Doped Graphene and Its Applications

method	precursors	doping structure	doping level	applications, refs
CVD	ethanol, boron powder	graphitic B (BC_3), boron silane (BC_2)	0.5 at. %	105
	methane, diborane	sp^2 C−B, C_2−BO, C−BO_2, and B_2O_3	1.5−2.5 at. %	111
	phenylboronic acid	mainly BC_3	1.5 at. %	112
	CH_4, H_2, B_2H_6 gases	graphitic B	10×10^{12} cm^{-2}	108
	CH_4, B powder	B_4C, graphitic B, B oxycarbides	3.2 at. % (surface)	113
thermal annealing	graphite with H_2BO_3	B cluster/B carbide, graphitic N	4.46 at. % + 0.22 at. %	109
thermal exfoliation	graphite oxide, BF_3 in N_2/H_2		23, 140, 590 ppm	ORR[193]
liquid process	B-containing polycyclic aromatic hydrocarbon	graphitic B	58 ppm	110
	GO, borane−tetrahydrofuran adduct	B−C	0.7−1.1 at. %	supercapacitor[114]
	graphene, borane tetrahydrofuran	B−C	1.85%	HER[239]
arc discharge	graphite electrode with H_2, He, and B_2H_6	graphitic B	1.2−3.1 at. %	88
microwave plasma	graphene, trimethylboron	sp^2-bonded B	0−13.85 at. %	103
Wurtz-type reductive coupling reaction	CCl_4, K, BBr_3	sp^2 bonding, BC_3	2.56 at. %	107

In situ CVD was also explored to prepare NG using C- and N-containing gases or small molecules.[85,93−98] Luo et al. synthesized monolayer NG via CVD using H_2, C_2H_4, and NH_3 on Cu foils, with up to 16 at. % of pure pyridinic N, which provides a platform to study the doping effect of one specific N configuration on the physical, chemical, and electronic properties of graphene.[93] Usachov et al. prepared triazine-derived NG, which shows a bandgap of 0.3 eV and concentration of charge-carriers of $\sim 8 \times 10^{12}$ electrons/cm^2 induced by 0.4 at. % of graphitic N.[96] Interestingly, the N-doping structure can be changed from pyridinic to graphitic N by post-annealing of N-graphene after gold intercalation.

A facile liquid process has been proposed to prepare NG.[82,84,99,100] Bao's group has developed a solvothermal synthesis of NG by reacting tetrachloromethane with lithium nitride under mild conditions, and obtained NG samples with the N/C ratio up to 16.4%.[82] Significantly, the N doping was directly observed by scanning tunnelling microscopy (STM): the STM images show brighter sections with sizes smaller than 0.5 nm originating from C atoms near doped N species because of the increased electron density. Yoon's group reported a hydrothermal method to simultaneously perform N doping and reduce GO to graphene in the presence of NH_3 and N_2H_4.[99] A supercritical reaction in acetonitrile was also proposed by Qian et al. to synthesize NG using an expanded graphite, which resulted in the N-doping level reaching up to 4.56 at. %.[100]

Various methods have been reported for the synthesis of NG.[88,90,101,102] Rao et al. prepared NG by arc discharge using graphite electrodes in the presence of pyridine/ammonia in H_2 atmosphere.[88] Shao et al. obtained NG by exposing graphene to N_2 plasma, in which pyridinic, pyrrolic, and graphitic N, and N oxides of pyridinic N were generated.[90] Zhao's group indicated that NG can be obtained by low-energy nitrogen bombardment of graphene on Ni(111) using ion energies between 25 and 100 eV.[101]

2.2. B-Doped Graphene (BG). *2.2.1. B-Doping Configurations.* Doing graphene with B ($2s^22p^1$) has been shown to be energetically favorable because the formation energy of BG in the case of gaseous dopant is ~5.6 eV/atom, much lower than that of N-doping (8.0 eV/atom).[103] For in-plane doping, B atoms in the carbon lattice are sp^2-hybridized, allowing retention of the planar structure of graphene due to the similarities between B and C atoms; however, the lattice parameters are slightly altered because the B−C bond (~1.50 Å) is longer than the C−C bond (1.42 Å). In contrast to the in-plane B-doping, the B-doping at the vacant sites with a tetrahedral-like BC_4 unit in which all the dangling carbon atoms are saturated, causes some distortion of the graphene planar structure, but all of the out-of-plane starting positions would relax to the same in-plane position because of its instability.[104] Furthermore, two in-plane binding structures in BG were observed by Zhu's group (Figure 2a,b): the graphitic-B at 200.5 eV in the XPS spectrum referring to the B atoms replacing C atoms in the hexagonal ring, and the "boron silane" B at 198.5 eV, which refers to B atoms located in a π-conjugated system.[105]

2.2.2. B-Doping Effect. With one less valence electron to the neighboring C, the B-doping induces a charge polarization in the graphene matrix (becomes negatively charged), which is favorable for electrocatalysis, and p-type behavior by down-shifting the Fermi level toward the Dirac point (Figure 2c−f).[104−106] By tuning the B-doping level, different bandgaps of BG from 0 to 0.54 eV can be induced (Figure 2e).[103] The enhanced conductivity was observed because graphitic B-doping provides more holes to the valence band of graphene, which results in increasing the carrier concentration in BG (~0.5 carriers per dopant); it would even likely become a superconductor if the doping level increases to 4−5 at. %,[88,107−109] whereas the "boron silane" B contributes one p electron to the π-conjugated system.[105] The broad absorption over the entire visible region as well as fluorescence in the near-IR region was found in BG, which can be attributed to the p orbitals in B atoms contributing to both the relevant unoccupied and occupied orbitals.[110]

2.2.3. Methods for Synthesis of BG. Table 2 summarizes the main methods available in the literature for the synthesis of BG. The thermal annealing process at 2450 °C was adopted to prepare BG using graphite and H_2BO_3, supplemented by mechanical exfoliation.[109] Raman spectroscopy was used to verify the B doping, which is reflected by the 7-fold increase in the intensity of D band (I_D; intensity of other peaks are denoted similarly) as well as the equality of $I_{D'}$ and $I_{G'}$; further, it was indicated that the B atoms are, on average, spaced 4.76 nm apart in the graphene layer.

In situ CVD has been widely utilized to synthesize BG using C-containing or B-containing gas/solid precur-

DOI: 10.1021/acscatal.5b00991
ACS Catal. 2015, 5, 5207−5234

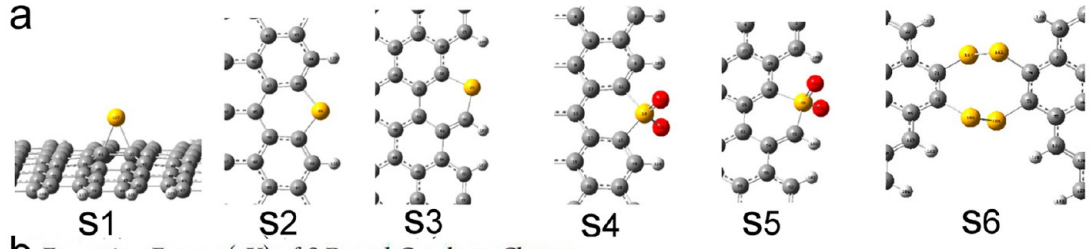

b Formation Energy (eV) of S-Doped Graphene Clusters

graphene clusters	surface adsorption P 1	surface adsorption P 2	zigzag edge substitution	armchair edge substitution	SO_2- zigzag edge substitution	SO_2- armchair edge substitution	ring clustering
without defect	−1.46	−1.73	0.90	2.02	1.47	2.73	2.70
with defect	−2.60	−2.31	0.89	1.80	1.44	2.37	2.54

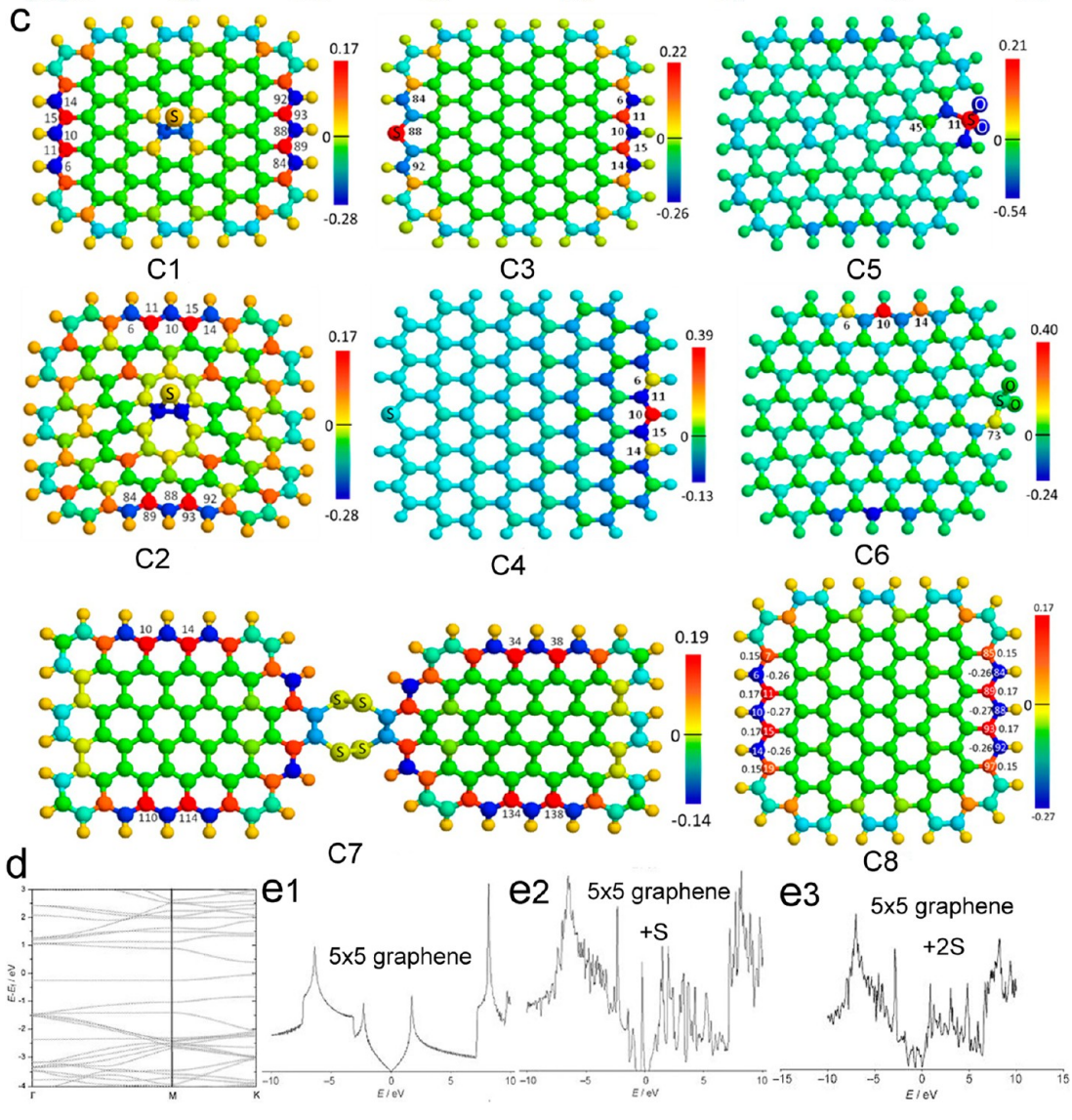

Figure 3. (a) S-doped configurations: S atoms adsorbed on graphene surface (S1), substituting S atoms at zigzag (S2) and armchair edges (S3); SO_2 substituted at zigzag (S4) and armchair edges (S5), S ring cluster connecting two pieces of graphene (S6). Small white, gray, yellow, and red balls represent H, C, S, and O atoms, respectively. (b) Formation energy (eV) of SG clusters. (c) Atomic charge density distribution of S1-graphene with (C1) perfect structure and (C2) one Stone−Wales defect; (C3) atomic charge density and (C4) spin density distributions on S2-graphene; (C5) atomic charge density and (C6) spin density on SO_2-doped graphene with a Stone−Wales defect; atomic charge density on (C7) S5-graphene and (C8) pure graphene cluster. The colors of the balls stand for relative values of charge and spin density. The density decreases linearly from positive to negative values in the color order of red, orange, yellow, green, and blue. Sulfur and oxygen atoms are labeled with S and O, respectively. The unlabeled small and large balls represent H and C, respectively. Reproduced with permission from Xia et al.[116] Copyright 2014, American Chemical Society. (d) Band structure determined for 5 × 5 graphene doped with one S atom. (e1−3) DOS determined for pristine graphene, singly S-doped 5 × 5 graphene (2 at. %), and dual S-doped 5 × 5 graphene (4 at. %). Reproduced with permission from Mombru et al.[115] Copyright 2009, Wiley VCH.

DOI: 10.1021/acscatal.5b00991
ACS Catal. 2015, 5, 5207−5234

Table 3. Summary of Sulfur-Doped Graphene and Its Applications

method	precursors	doping structure	doping level	applications, refs
thermal annealing	GO, BDS	−C−S−C−, −C−SO_x−C−	1.30−1.53%	ORR[120]
	GO, $MgSO_4$	−C−SO_x−C−, thiophene S	2.56 at. %	121
	GO, phenyl disulfide		2.1 at. %	ORR and methanol oxidation reaction[122]
	3D SG: GO, dibenzyl disulfide	−C−S−C−, −C−SO_x−C−	0−1.99 at. %	ORR[196]
	graphene, CS_2 vapor	thiophene S and −C−SO_x−C−	0.73−2.0 at. %	ORR[194]
thermal exfoliation	graphite and H_2S, SO_2, CS_2 gases	−C−S−	0.75−7.03 wt %	ORR[118]
solvothermal method	3D SG: GO, Na_2S	thiophene S	0.5 at. %	ORR[197]
	SG QDs: fructose, sulfuric acid	thiophene S, oxide S	1 at. %	123
	GO, BDS	thiophene S	1.2 at. %	119
	GO, BDS	thiophene S	2.3 at. %	ORR[124]
ball-milling	graphite, sulfur	major C−S, minor $-SO_3H$	4.94 at. %	ORR[117]
electrolysis in 5 V	SG QDs: graphite, sodium p-toluenesulfonate	−C−S−C−, −C−SO_2−C−	4.25%	127
cycled lithium−sulfur battery	graphene S composites	C═S, C−S bonds, −C−SO_x−C−		125
ion-exchange/activation combination method	3D SG: 732-type sulfonic acid ion-exchange resin	C═S, C−S bonds, −C−SO_x−C−	12.8 wt %	ORR[126]

sors.[105,108,111−113] Wang et al. prepared BG with 1.5 at. % of graphitic B via CVD using phenylboronic acid as the sole precursor. The obtained BG exhibited a pronounced D band (1351 cm^{-1}) and an accompanied D′ band (1620 cm^{-1}) with an $I_D/I_G \sim 1.9$ on the Raman spectrum, which can be explained by the elastically scattered photoexcited electron generated by heteroatom-doping and intravalley double resonance scattering processes. Further, the G band (1592 cm^{-1}) and 2D band (2695 cm^{-1}) of BG show upshifts of 6 and 9 cm^{-1}, respectively; meanwhile, I_{2D}/I_G decreases.[112]

A facile reflux process was also developed to produce BG on a large scale by reduction of GO in borane−tetrahydrofuran solution, obtaining a BG material with a high specific surface area of 466 $m^2\ g^{-1}$ and B doping level of 1.1 at. %.[114] Interestingly, a rapid Wurtz-type reductive coupling reaction was also explored by Lü and colleagues to prepare BG with graphitic B using tetrachloromethane, potassium, and BBr_3 at 150−210 °C for 10 min.[107] Moreover, Dou's group got BG via a bottom-up organic synthesis using B-containing polycyclic aromatic hydrocarbon.[110] Microwave plasma was also applied to synthesize BG using trimethylboron, which allows tuning the doping level up to 13.85 at. % by extending duration of the reaction to 20 min.[103] A detailed inspection of the B K-edge in electron energy loss spectroscopy shows a sharp π^* peak as well as a board σ^* band, suggesting that B atoms are in the sp^2-hybridized state (graphitic B). According to the XPS analysis of BG, as the reaction time increases, the C 1s spectra become asymmetric, with an increasing C−B peak intensity, and the B−C bond in the B 1s spectra gradually shifts to a higher B.E.[103]

2.3. S-Doped Graphene (SG). *2.3.1. S-doping configurations.* The C−S bond length (1.78 Å) is ∼25% longer than that of the C−C bond; thus, the S-doping gives a stable structure in which each S atom is ∼1.1 Å above the graphene plane.[115] Using the DFT method, Xia et al. showed that there are four types of S atoms in SG: namely, S could be adsorbed on the graphene surface (S1), substitute for C atoms at edges (S2 and S3) in the form of S/S oxide (S4 and S5), or connect two graphene sheets by forming a S cluster ring (S6, Figure 3a).[116] According to the formation energy, adsorption of S on graphene results in the most stable structure; S prefers to substitute C atoms at the zigzag edge, and the Stone−Wales defects can facilitate S-doping because of the changed local charge distribution in the C lattice (Figure 3b).[116]

2.3.2. S-Doping Effect. Unlike previously discussed N and B doping effects, a negligible polarization (or charge transfer) exists in the C−S bond because of the similar electronegativities of S (2.58) and C (2.55). However, S atoms substituting for C atoms at the graphene edges (S2, S3, S4, and S5) exhibit high charge and spin densities, and S6 shows a smaller value, whereas no spin density is observed in pristine graphene and S-adsorbed graphene (S1, Figure 3c).[116,117] The degeneracy of the two bands at the Fermi level is lifted in the band plot of SG with one S atom (Figure 3d), and a band gap of 0.3 eV is observed in the doped graphene with one S atom, but that with two S atoms increases the metallic properties of graphene (Figure 3e).[115] Pumera's group reported that the majority of the S-doped samples showed higher resistivity than their undoped counterparts, which was attributed to the trapping of free carriers by the S and O functionalities.[118] In contrast, Wang et al. indicated that the thiophene S doping (S2 and S3) can enhance graphene conductivity due to its stronger electron donor ability and more effective reduction caused by S doping.[119]

2.3.3. Methods for Synthesis of SG. Table 3 summarizes the main methods available in the literature for the synthesis of SG. Because incorporation of S atoms into graphene requires a higher energy of formation than that in the case of N or B atoms, the synthesis of SG is more difficult. SG can be prepared by thermally annealing GO and S-containing precursors at high temperatures.[120−122] Li et al. synthesized porous SG via thermal annealing using sulfate ($MgSO_4$) in N_2 at above 700 °C, in which the oxide S doping can be decomposed and the remaining S is transformed into electrochemical active thiophene S.[121] In addition, the liquid method was reported to obtain SG.[123,124] Liu and colleagues obtained SG with pure thiophene S bonding using GO and benzyl disulfide (BDS) by a rapid microwave-assisted solvothermal method, assuring an S-doping level of 2.3 at. % in 6 min.[124]

SG can also be obtained during exfoliation of graphite in the presence of S sources.[117,118] Baek's group reported a simple ball-milling method to synthesize an edge-sulfurized graphene using pristine graphite and sulfur (S_8).[117] Pumera's group prepared SG by thermal exfoliation of graphite oxide in H_2S, SO_2, or CS_2 gases; in this case, the doping level is dramatically influenced by the type of graphite oxide (prepared by different methods) rather than the S-containing gas.[118] Other methods

DOI: 10.1021/acscatal.5b00991
ACS Catal. 2015, 5, 5207−5234

have been also reported, such as cycled lithium−sulfur batteries using graphene−sulfur composites as cathode materials and a combined ion-exchange/activation method.[125−127]

2.4. P-Doped Graphene (PG). *2.4.1. P-Doping Configurations.* P ($3s^2 3p^3$) has the same number of valence electrons as N but a fundamentally different doping effect because of the additional orbital and higher electron-donating ability than N, that the P atom has a charge of 5.25 e^- as compared with that of N (4.39 e^-).[128] Moreover, the electronegativity of P (2.19) is lower than that of C; thus, the polarity of the C−P bonding is opposite to that of the C−N bonding.[129] In PG, a strong hybridization between P 3p and C 2p orbitals transforms the sp^2 C into the sp^3 hybridization, forming a pyramidal-like bonding configuration with three C atoms (Figure 4a).[130,131] In this configuration, P overhangs from the graphene plane by 1.33 Å, which is associated with an ∼25% increase in the P−C bond length (1.77 Å) with respect to the C−C bond length, thus causing structural distortion and inducing defect sites in the graphene sheet and consequently reducing the electroconductivity.[129,130,132]

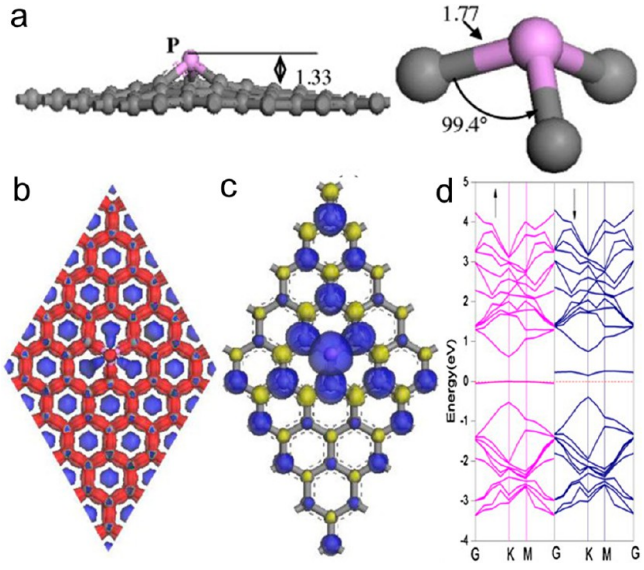

Figure 4. PG: (a) The P-doping configuration. The gray and pink balls represent C and P atoms. (b) The charge density distribution, in which the red and blue regions represent the areas of electron accumulation and loss. (c) The spin density state. (d) Computed band structures. Reproduced with permission from Wang et al.[130] Copyright 2013, Elsevier.

2.4.2. P-Doping Effect. According to calculations, the different electron affinities of P and C atoms result in some transformation of the charge density in PG; ∼0.21 e^- is transferred from the P dopant to the graphene matrix, making PG an n-type material (Figure 4b).[130] Because the π system of graphene is broken, a magnetic moment of 1.05 μ_B is induced in the PG, and its spin state is distributed over the whole graphene surface (Figure 4c).[130,131] Further, the minimum of the conduction band edge of graphene is found to be slightly shifted up, forming a small bandgap of 0.15 eV, as compared with that of pristine graphene (Figure 4d).[130]

2.4.3. Methods for Synthesis of PG. Table 4 summarizes the main methods for the synthesis of PG. García et al. reported an in situ synthesis of PG by the pyrolysis of a natural alginate conjugated with $H_2PO_4^-$ in O_2 at 900 °C. The resulting PG possessed P−O and P−C bonds as well as an optical bandgap of 2.85 eV.[133] PG can also be obtained by post-thermal annealing synthesis using graphene/GO with P-containing precursors under a protecting atmosphere.[134−137] Some et al. prepared PG by annealing graphene with triphenylphosphine (TPP) in Ar at 100−250 °C. The resulting PG exhibited P−C bonding and a doping level of 4.96 at. %.[134] Li et al. used a mixture of GO and ionic liquid (1-butyl-3-methylimidazolium hexafluorophosphate) to prepare PG with P−C and P−O bonds, also by annealing.[135] A partial oxidation of P atoms is caused by the active oxygen released from GO during a thermal process, forming covalently bonded tetrahedral structures such as C_3PO, C_2PO_2, and CPO_3, thus resulting in a charge redistribution in PG.

Pumera et al. investigated the effect of the doping source in the liquid synthesis of PG.[138] It was found that only P_4 and PH_3 can ensure a successful P-doping into the graphene matrix; in this case, P_4 is a better dopant source than PH_3 because the latter gives a total P 2p content of only 0.10%. Hypophosphite and phosphite act as reducing agents only in the synthesis process. PG obtained by using P_4 as a doping source exhibits both P−C and P−O bonds, whereas that prepared with the aid of KOH contains P−C bonding only with a doping level of 3.65 at. %.

2.5. Double-Doped Graphene. Table 5 summarizes the main methods for the synthesis of double-doped graphene.

2.5.1. B and N-Doped Graphene (BNG). Through DFT calculations, Sen et al. demonstrated that codoping graphene with N and B atoms can further increase the efficiency of N-doping as a result of the stabilization provided by B−N bonding.[139] Experimentally, BNG has been synthesized using various methods.[140−145] Antonietti's group has reported an in situ pyrolytic synthesis of holey BNG monoliths by direct copolymerization of glucose and boric acid in the interlayer spaces of lamellar carbon nitride.[140] On the basis of the XPS analysis, ∼16 at. % of doped N is in the form of pyridinic and

Table 4. Summary of Phosphorus-Doped Graphene and Its Applications

method	precursors	doping structure	doping level	applications, refs
thermal annealing	graphene, TPP	P−C bonding	4.96%	FETs[134]
	$H_2PO_4^-$-modified alginate	P−C, P−O	2.56 at. %	107,133
	GO, an ionic liquid 1-butyl-3-methlyimidazolium hexafluorophosphate	P−C, P−O	1.16 at. %	ORR[135]
	graphite oxide, TPP	P−C, P−O	1.81 at. %	ORR[136]
	GO/graphene with phosphoric acid	P−C, pyrophosphate, metaphosphate	1.30 at. %	137
liquid process	GO with P_4, PH_3	P_4: P−C with the existence of KOH; 79.8% of P−C and 20.2% of P−O without KOH	P_4, 3.65 at. %; PH_3, 0.10%	138

DOI: 10.1021/acscatal.5b00991
ACS Catal. 2015, 5, 5207−5234

Table 5. Summary of Double-Doped Graphene and Their Applications

doping type	method	precursors	doping structure	doping level	applications, refs
B-, N-doped graphene	thermal annealing	GO, B_2O_3, NH_3	B: B−C, B−N; N: N−B, N−C	B/C 0.6−1.2 at. %; N/C: 0.5−1.3 at. %	141
		GO, CO_2, NH_3BF_3	BCO_2, pyrrolic N	B: 6.33−26.66 at.%; N: 11.44−26.98 at. %	ORR[142]
		glucose, boric acid	N: pyridinic, graphitic, N−B bonds; B: C−B, N−B, B−O bonds	B: 14 at. %; N: 16 at. %	140
		graphene, NH_3, H_3BO_3	N: pyridinic, pyrrolic, graphitic; B: BC_3	N: 2.03 at. % of pyridinic, 1.29 at. % of pyrrolic, 0.90 at. % of graphitic; B: 2.17 at. % of BC_3.	ORR[143]
		graphene/GQDs: GO, solid boric acid, NH_3	N: N−B, pyridinic, pyrrolic, graphitic N; B: N−B−C, BCO_2	B: 13.6 at. %; N: 18.3 at. %	ORR[200]
	CVD	urea, boric acid, polyethylene glycol	N: B−N, pyridinic C−N, pyrrolic C−N, graphitic C−N, oxidic O−N; B: C−B, N−B, O−B bonding	N: 5.64−13.07 at. %; B: 1.23−6.85 at. %	ORR[146]
	hydrothermal reaction	3D aerogel: GO, NH_3BF_3	pyridinic, pyrrolic, graphitic N; C−N−B	N: ∼3.0 at. %, B: ∼0.6 at. %	supercapacitor[148]
	electrochemical preparation	GO, ethylenediamine + 1,4 phenylenebis(boronic acid) in phosphate buffer solution	B−C(sp^2) bond, G-BN, G-BNO, G-BO_2	B: 5.2 at. %; N: 4.7 at. %	ORR[145]
P-, N-doped graphene	CVD	CH_4, $(NH_4)_3PO_4$	P: P−C and P−O; N: pyridinic, pyrrolic, graphitic N	P: 0.6 at. %; N: 2.6 at. %	lithium ion batteries[160]
		ethanol, phosphonitrilic chloride trimer	P: P−C and P−O; N: pyridinic, pyrrolic, graphitic N	N: 1.50−4.05%; P: 0.65−2.45%	161
	thermal annealing	GO, melamine, TPP	P: P−3C(−O); N: pyridinic, pyrrolic, graphitic, N−O(C)	N: 4.60%; P: 1.63%	HER[243]
S-, N-doped graphene	thermal annealing	GO, melamine, BDS	S: thiophene S; N: pyridinic, pyrrolic, graphitic N	N: 4.5 at. %; S: 2.0 at. %	ORR[151]
		GO, 2-aminothiophenol	N: pyridinic, pyrrolic N; S: thiophene S	N: 1.76%; S: 0.86%	lithium ion batteries and ORR[152]
		GO, thiourea	N: pyridinic, pyrrolic, graphitic; S: C−S−C.	N: 2.02 at. %; S: 2.54 at. %	solar cells[155]
		graphite oxide, poly[3-amino-5-mercapto-1,2,4-triazole]	N: pyridinic, pyrrolic, graphitic N; S: thiophene S, oxidized S	N: 0.89−1.25%; S: 0.17−0.34%	ORR[156]
		GO, thiourea	N: pyridinic, pyrrolic, graphitic N; S: C−S, −C═S−, $-SO_n-$	N: ∼7.8−3.4%; S: ∼1.05−1.4%	ORR[157]
		GO, polydopamine, cysteine	N: graphitic, pyrrolic, pyridinic N; S: thiophene S, S−O species	N: 2.12%; S: 1.70%	ORR[154]
	CVD	pyrimidine, thiophene	S: −C−S−C−, little $-C-SO_x-C-$; N: pyridinic, pyrrolic/graphitic N	N: 3.7−5.7%; S: 0.7−2.0%	ORR[149]
		pyridine, thiophene	N: graphitic, pyridinic, oxide N; S: −C−S−C−, −C═S−, −C−SO−, $-C-SO_2-$	N: 3.79−2.55%; S: 5.06−0.56%	HER[150]
	reflux	GO, Chinese wolfberry/inulin	N: pyridinic, pyrrolic, graphitic N; S: thiophene S, oxidized S	N: 2.8/2.9%; S: 0.26/0.11%	158
	hydrothermal reaction	GO, mercapto acetic acid, DL-penicillamine	N: pyridinic, graphitic N; S: $C-S_n-C$ (n = 1, 2), $C-SO_x-C$ (x = 2, 3, 4)	N: 2.12 at. %; S: 8.92 at. %	solar cells[159]

DOI: 10.1021/acscatal.5b00991
ACS Catal. 2015, 5, 5207−5234

graphitic N, and the N−B bonds were detected, too, whereas the doped B atoms appear mainly in the C−B and N−B bonds and to a smaller degree in the B−O bonding with a doping level of 14 at. %. It was shown that B atoms (as electron acceptors) and N atoms (as electron donors) could lower the valence band and elevate the conduction band that results in electron relocalization and activation of graphene. In particular, the bond structure was found to depend on the preferentially doped N configuration in the BNG obtained by CVD.[146] By substituting the in-plane C atom with all its electrons configured into the π electron system of graphene with N, the formation of B and N in the separated states is preferred. In contrast, when the edge-plane carbon is substituted with N, it favors the formation of the B−N structure. Importantly, the former structure shows an excellent ORR performance in alkaline solutions due to the synergistic effect between B and N, and the latter shows graphite-like activity for ORR.[144,147]

The postsynthesis treatment of BNG has also been extensively studied.[141,143,144,148] Lin et al. prepared BNG by reacting GO with B_2O_3 and NH_3 at 900 to 1100 °C. B and N atoms were incorporated into the graphene lattice in the form of randomly distributed BN nanodomains, contributing to an ambipolar semiconductor behavior with a bandgap of ∼25.8 meV.[141] Most of the synthetic strategies of BNG inevitably lead to undesired byproducts such as hexagonal boron nitride (*h*-BN). Significantly, our group obtained a *h*-BN-free BNG by a two-step doping method, in which N was first doped by annealing GO with NH_3 at a modest temperature (e.g., 500 °C) and then B was introduced with H_3BO_3 at a higher temperature (e.g., 900 °C).[143] It was found that N atoms were in pyridinic (∼2.03 at. %), pyrrolic (∼1.29 at. %), and graphitic N forms (∼0.90 at. %), without any N−B configuration, and all B atoms were bonded to C atoms in the form of a BC_3 structure (∼2.17 at. %) without forming the undesirable *h*-BN.

Interestingly, Müllen's group reported the hydrothermal synthesis of 3D BNG aerogel using GO and NH_3BF_3, in which 3.0 at. % of N in the form of pyridinic, pyrrolic, and graphitic N and C−N−B bonds and 3.0 at. % of B were detected.[148] This aerogel consisted of well-interconnected ultrathin graphene sheets providing a high surface area, 3D macroporosity, and high electrical conductivity favorable for ion and electron transport.

2.5.2. S and N-Doped Graphene (SNG). The in situ CVD synthesis of SNG was demonstrated very recently.[149,150] Guan et al. obtained SNG at 700 °C using pyrimidine and thiophene as pyrolytic precursors, in which S-doping occurred mainly in the form of sulfide groups (−C−S−C−) and, to a smaller degree, in the form of oxidized S groups (−C−SO_x−C−) with pyrrolic/graphitic N structures.[149] Chen's group synthesized nanoporous SNG using nanoporous Ni as both the template and substrate and pyridine and thiophene as C, N, and S doping sources, respectively.[150]

SNG prepared through the postannealing process has been extensively studied.[151−157] We prepared macroporous SNG by annealing GO at 900 °C in Ar using melamine and BDS as the doping sources and colloidal silica spheres as the hard template.[151] The S-doping level was 2.0 at. % with pure thiophene S bonding; and the N-doping level was 4.5 at. % in the form of pyridinic, pyrrolic, and graphitic N. Wang et al. indicated that the doping level in SNG was dependent on the reaction temperature; namely, the overall content of S and N dopants decreased with increasing temperature, with the N content decreasing and S content increasing, indicating that an effective S doping requires higher temperature.[153] In addition, the liquid phase synthesis of SNG was also reported.[158,159] For example, Luo and colleagues reported a hydrothermal synthesis of SNG using GO and mercaptoacetic acid and DL-penicillamine as doping sources, resulting in 2.12 at. % N and 8.92 at. % S doping levels.[159]

2.5.3. P and N-Doped Graphene (PNG). Theoretically, Terrones and colleagues demonstrated that the heteroatomic PN defect is more stable than the P defect in PNG because the N dopant helps to reduce the displacement caused by inclusion of P, thus resulting in a "damping" effect on the structural distortion, especially within the first and second neighbors.[129] Porous PNG networks were synthesized by Ma's group via a MgO-templating in situ CVD process using CH_4 and $(NH_4)_3PO_4$ as N and P sources at 900 °C in Ar.[160] The XPS analysis indicated that 0.6 at. % of P atoms were covalently bonded with C in the tetrahedral forms, such as C_3−PO, C_2−PO_2, and C-PO_3, whereas 2.6 at. % of N atoms were present in the form of pyridinic, pyrrolic, and graphitic N. An increase in the amount of defects or disorders was observed after P−N doping, according to the Raman spectra.

The double-doping configuration, level, and effect were analyzed in relation to the synthesis temperature for the CVD-synthesized PNG, which exhibited remarkable air-stable n-type characteristics, with the electron mobility reaching 8−15 $cm^2 V^{-1} s^{-1}$.[161] For the N-doping configuration achieved at 700 °C, the amount of different N species followed the following order: pyridinic N > pyrrolic N > graphitic N. For PNG prepared at 800 °C, N existed in the form of pyrrolic and graphitic N with similar content; for PNG obtained at 900 °C, graphitic N species were mainly present, and the amount of pyrrolic N was very small; and PNG obtained at 1000 °C exhibited N only in the form of graphitic N. For P dopants, the amount of P−C bonds increased and that of P−O bonds decreased with an increase in the temperature from 700 to 1000 °C, suggesting that higher temperatures benefit the effective doping with P atoms. The doping levels for both P and N atoms were found to decrease as a function of temperature, with the N-doping level always being higher than that of P doping. In contrast, the doping effect increased with the temperature because of the formation of more-stable bond configurations by dopants at higher temperatures.

In addition, ternary-doped graphene has also been reported by Yu and colleagues as ORR catalysts, using GO as the precursor, thiourea as the source of N and S, and TPP as the P source through a thermal-annealing process at 800 °C in N_2.[162] Interestingly, the P doping can help to create more pyridinic N and pyrrolic N in SNG by formation of P═N and P−N bonds; the S-doping level is lower than that of N doping because there is only one binding configuration of thiophene S.

2.6. Other Doping Types. Doping graphene with other heteroatoms has been also studied.[163,164] By adding H into a graphene matrix, a stable 2D hydrogenated graphene (also called graphene) in which the sp^2 C is transferred to sp^3 C is formed.[164] Depending on the amount of H coverage on the graphene surface, a tunable bandgap can be induced, reaching values as high as 5.4 eV, and an n-type behavior can be observed in graphene. On the other hand, halogen atoms can also be doped into graphene, resulting in drastic geometric and electronic distortions in graphene sheets.[163] The F−C bond in F-doped graphene sticks out from the graphene basal plane and stretches the C−C bond length to 1.57−1.58 Å. With full coverage of F atoms on graphene, fluorographene is formed by

DOI: 10.1021/acscatal.5b00991
ACS Catal. 2015, 5, 5207−5234

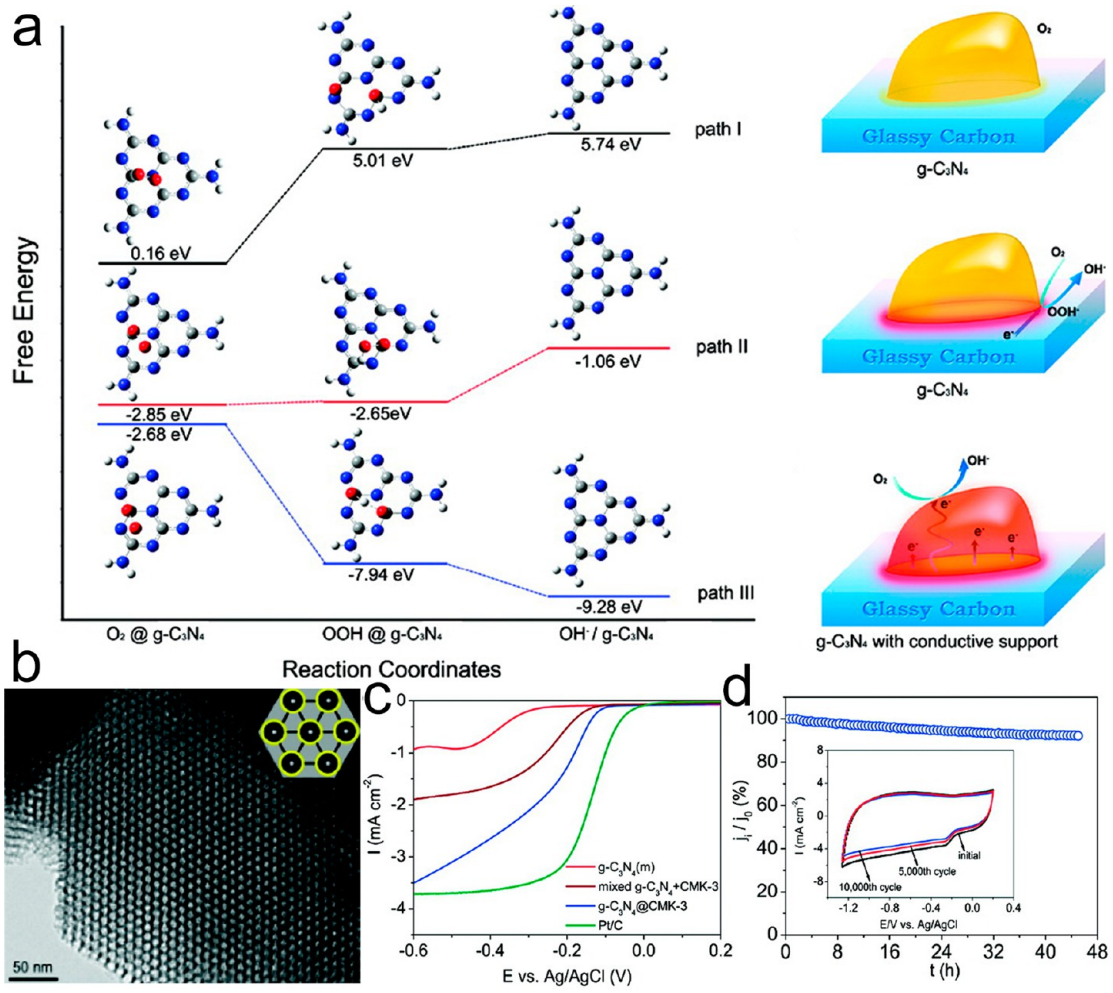

Figure 5. (a) Left side: free energy plots of ORR and optimized configurations of adsorbed species on the g-C_3N_4 surface with 0 e^-, 2 e^-, and 4 e^- participation demonstrated as paths I, II, and III. Energy levels are not drawn to scale. Gray, blue, red, and white small spheres represent C, N, O, and H, respectively; Right side: schemes of the ORR's pathway on pristine g-C_3N_4 without electron participation, pristine g-C_3N_4 with 2 e^- participation, and g-C_3N_4 on conductive support composite with 4 e^- participation, respectively (red areas represent the active sites facilitating ORR). (b) TEM image of ordered mesoporous g-C_3N_4@CMK-3 nanorods. Inset represents a schematic illustration (yellow, g-C_3N_4; black, carbon). (c) Linear sweep voltammograms (LSVs) of various catalysts at 1500 rpm in O_2-saturated 0.1 M KOH; (d) Current−time (i−t) chronoamperometric response of g-C_3N_4@CMK-3 at −0.3 V; inset represents cyclic voltammograms (CV) under continuous potentiodynamic sweeps. Reproduced with permission from Qiao et al.[176] Copyright 2011, American Chemical Society.

sandwiching a graphene basal plane between two F layers, making the resulting structure the thinnest insulator, with a bandgap of ∼3 eV due to a high degree of sp^3 C. The Cl-doped graphene has a longer bond length; thus, it has a larger thickness than FG. The large-sized Br and I were reported to interact with graphene only via physisorption or charge transfer complex formation, which do not disrupt the sp^2 C network. The I-doped graphene was prepared by Yao et al. by annealing GO and iodine at 500−1100 °C in Ar, which displayed a greater ORR electrocatalytic activity than Pt/C by the formation of an I_3^- structure.[163]

3. ORR ELECTROCATALYSTS

The ORR proceeds via either a direct four-electron ($4e^-$) pathway or a two-step, two-electron ($2e^-$) pathway under both acidic and alkaline conditions.

Direct $4e^-$ pathway:

$$O_2 + 2H_2O + 4e^- \rightarrow 4OH^- \quad (1, \text{alkaline})$$

Or

$$O_2 + 4H^+ + 4e^- \rightarrow 2H_2O \quad (2, \text{acidic})$$

Two-step $2e^-$ pathway:

$$O_2 + H_2O + 2e^- \rightarrow HO_2^- + OH^- \quad (3, \text{alkaline})$$

$$HO_2^- + H_2O + 2e^- \rightarrow 3OH^- \quad (4, \text{alkaline})$$

Or

$$O_2 + 2H^+ + 2e^- \rightarrow H_2O_2 \quad (5, \text{acidic})$$

$$H_2O_2 + 2H^+ + 2e^- \rightarrow H_2O \quad (6, \text{acidic})$$

The ORR performance can be evaluated by the onset potential, the electron transfer number (n), the kinetic-limiting current density (J_K), Tafel slope, etc. In particular, the n values per O_2 molecule involved in the typical ORR process can be calculated from the slope of the Koutecky−Levich (K−L) plots using the following equations:[55,165]

$$\frac{1}{J} = \frac{1}{J_L} + \frac{1}{J_K} = \frac{1}{B\omega^{0.5}} + \frac{1}{J_K} \quad (7)$$

DOI: 10.1021/acscatal.5b00991
ACS Catal. 2015, 5, 5207−5234

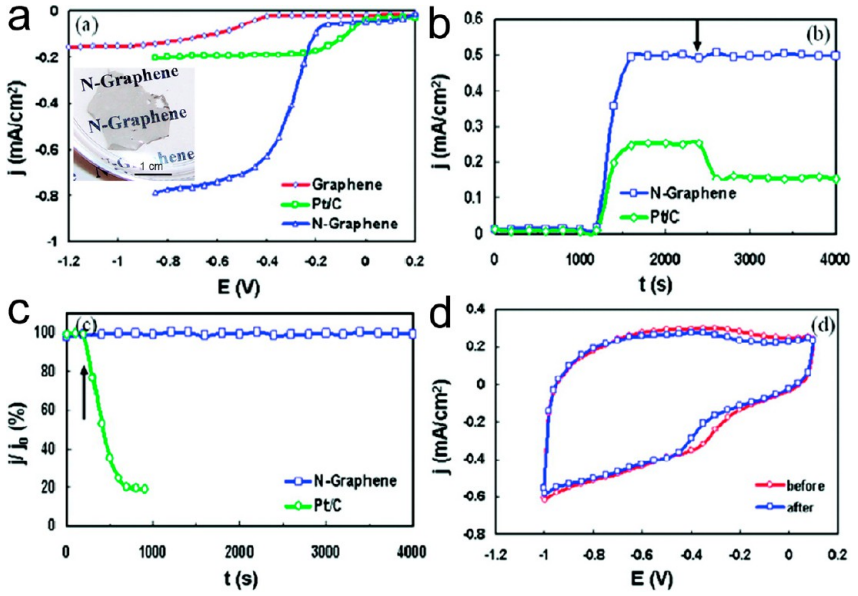

Figure 6. (a) RRDE voltammograms at the pristine graphene electrode, Pt/C electrode and N-graphene electrode. Electrode rotating rate: 1000 rpm. (b) Chronoamperometric responses obtained at the Pt/C and N-graphene electrodes at −0.4 V. The arrow indicates the addition of 2% (w/w) methanol into the cell. (c) Chronoamperometric response of Pt/C and N-graphene electrodes to CO at −0.4 V. The arrow indicates the addition of 10% (v/v) CO into the cell; j_0 is the initial current. (d) CV of N-graphene electrode before and after a continuous potentiodynamic swept for 200 000 cycles at 25 °C. All the tests were conducted in air-saturated 0.1 M KOH, with a loading mass of 7.5 μg and a scan rate of 0.01 V s^{-1}. Adapted with permission from Dai et al.[97] Copyright 2010, American Chemical Society.

$$B = 0.62nF\ C_0(D_0)^{2/3}\ \nu^{-1/6} \tag{8}$$

$$J_K = nFkC_0 \tag{9}$$

in which J is the measured current density, J_L is the diffusion-limiting current density, ω is the electrode rotating speed in rpm, B is the reciprocal of the slope, F is the Faraday constant (F = 96 485 C mol^{-1}), C_0 is the concentration of O_2, D_0 is the diffusion coefficient of O_2, ν is the kinematic viscosity of the electrolyte, and k is the electron transfer rate constant.

Furthermore, the n value can also be calculated by using rotating ring-disk electrode (RRDE) tests following the below equations.[55,165]

$$\%HO_2^- = 200 \times \frac{I_R/N}{I_D + I_R/N} \tag{10}$$

$$n = 4 \times \frac{I_R/N}{I_D + I_R/N} \tag{11}$$

where I_R and I_D are the ring and disk currents, respectively, and N is the collection efficiency (0.4) of the Pt ring.

3.1. Traditional ORR Catalysts. Noble metals are the most investigated traditional ORR catalysts.[32,166,167] Xu's DFT calculations indicated that the intrinsic ORR activity of Au, Ag, Pt, Pd, Ir, and Ru forms a volcano-like trend with respect to the adsorption energy of O_2, with Pt and Pd being the most active.[166] However, some unwanted side reactions always occur on the state-of-the-art Pt catalysts. For instance, some O_2^{2-} react with protons to create oxide species, which can block as much as 45% of Pt atoms and pull them off the electrode surface, consequently reducing its catalytic ability.[168] Stamenkovic's group[32] solved this problem by developing a $Pt_3Ni(111)$ alloy with an activity of 10-fold over a single-crystal Pt surface and 90-fold over the standard Pt/C because its unusual electronic structure and near-surface composition oscillation (between Pt and Ni) lower the electronic interaction between surface Pt atoms and the deleterious oxides, leaving more active sites open to carry out O_2-splitting reactions. Furthermore, Adzic and colleagues demonstrated that the Au clusters can improve the stability of Pt potential in the PtAu alloy by raising its oxidation, producing a similar change in the electronic behavior of the catalyst surface that prevents Pt atoms from dissolving into the electrolyte.[167]

In addition to the high cost, Pt is very sensitive to CO poisoning and methanol crossover; therefore, inexpensive catalysts with competitive ORR activity and resistance to CO/methanol poisoning have been explored, such as nonnoble metals, metal oxides, and sulfides, carbides, etc.[169−174] Deng et al. encapsulated Fe nanoparticles in the compartments of pea-pod-like CNTs, which exhibited good ORR activity as a result of efficient electron transfer from Fe to CNTs.[169] Our group has developed a metal−N−C catalyst (Fe−N−C in CNTs) combining the merits of its components, such as highly active Fe−N species for ORR, hierarchical porosity for facile reactant transportation, and sufficient active sites' exposure as well as high conductivity originating from graphitic CNTs.[171] Lee et al. reported a metal oxide-based ORR catalyst, in which Ketjen black carbon acted as a conductive support and amorphous MnO_x nanowires with rich surface defects were active sites for O_2 adsorption.[172] Dai's group developed a cobalt sulfide-graphene hybrid with good ORR performance related to the strong coupling between $Co_{1-x}S$ nanoparticles and conducting reduced graphene oxide (rGO) supports.[173] Hu et al. synthesized the Fe_3C/C hollow spheres with excellent ORR activity and stability in both acidic and alkaline media, in which the outer graphitic-C layers stabilize the Fe_3C nanoparticles under corrosive conditions while the inner nanoparticles activate the outer graphitic layers toward the ORR.[174]

Carbon-supported nonnoble-metal-based catalysts are inexpensive and active, but they still suffer from gradual

DOI: 10.1021/acscatal.5b00991
ACS Catal. 2015, 5, 5207−5234

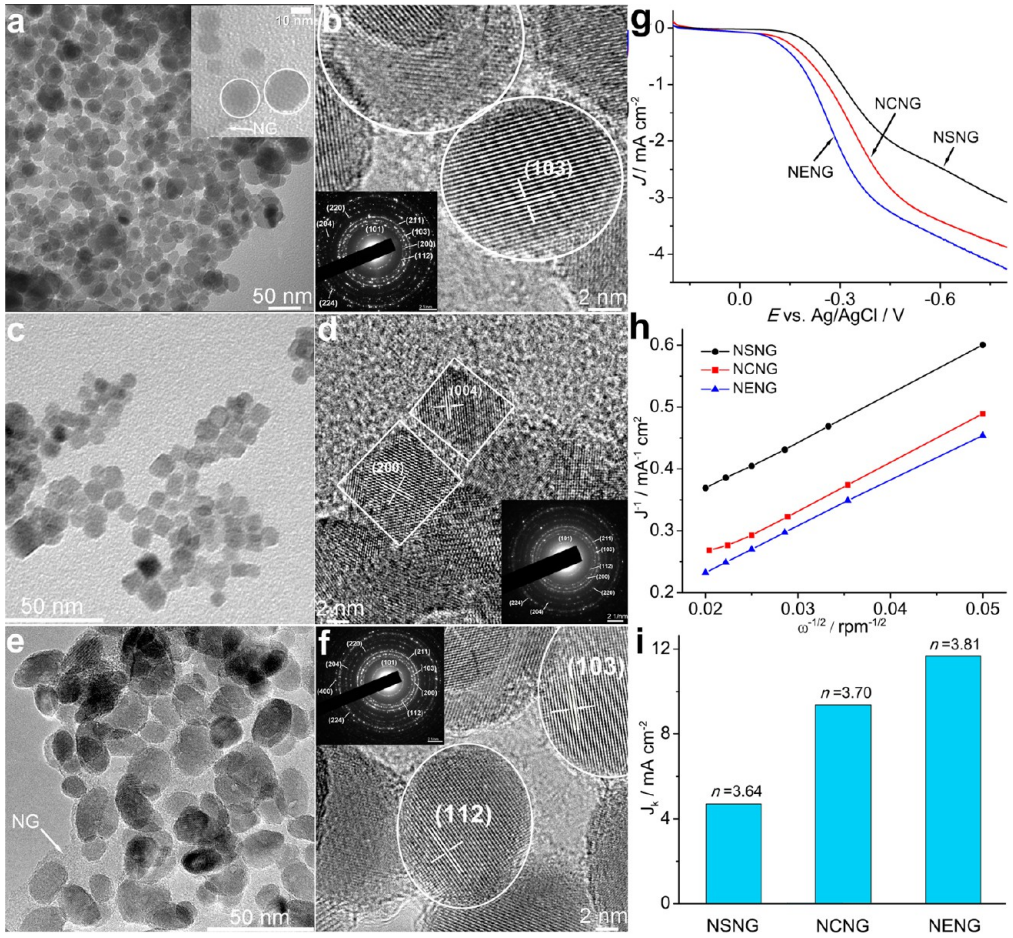

Figure 7. TEM images of Mn_3O_4/NG with nanoparticles as (a, b) spheres, (c, d) cubes, (e, f) ellipsoids. Insets are the electron diffraction patterns. (g) LSVs at a sweep rate of 5 mV s^{-1}. (h) Calculated K–L plots. (i) J_K and the n value. The tests were conducted in O_2-saturated 0.1 M KOH solution at −0.35 V vs Ag/AgCl. Catalyst loading was 0.1 mg cm^{-2} for all samples. Reproduced with permission from Qiao et al.[185] Copyright 2013. Wiley VCH.

deactivation during operation under corrosive conditions. Therefore, nonmetal materials such as heteroatom-doped carbon provide a promising solution.[175−177] Liming Dai's group reported vertically aligned nitrogen-containing CNTs, which displayed a good ORR activity, long-term operation stability and tolerance to methanol crossover effect in alkaline FCs because of the relatively high positive charge density of carbon atoms near the incorporated N.[175] Our group adopted g-C_3N_4, which has the highest N content among the N-containing C materials as ORR electrocatalysts with abundant active sites.[176,177] However, theoretical studies (Figure 5a) showed that O_2 cannot be reduced on the pristine g-C_3N_4 without electron participation (path I) because of the existence of two insurmountable barriers in the free energy plot of intermediate and final products. When 2 e^- are introduced (path II), the free energy of intermediate OOH@g-C_3N_4 decreases, indicating that the first 2 e^- reaction can proceed, but an obvious barrier still exists at the final state of OH^-/g-C_3N_4. This barrier can be eliminated by introducing 4 e^- (path III), by which most of the initially adsorbed O_2 molecules can be quickly reduced to OOH^- and directly form OH^- in the solution. Experimentally, we incorporated g-C_3N_4 into conductive CMK-3 to promote electron transfer in ORR, and the resultant g-C_3N_4@CMK-3 exhibited an excellent ORR activity with a nearly 100% 4 e^- pathway and a high stability with 92.2% preserved current after 45 h in alkaline solution (Figure 5b–d).[176]

3.2. Heteroatom-Doped Graphene Based Catalysts.

3.2.1. NG-Based Catalysts. Both theoretical and experimental studies indicate doping graphene with heteroatoms such as N, B, S, and P can improve the ORR catalytic activity, which may be attributed to the polarized distribution of spin and charge densities.[178,179] Our group reached the same conclusion and established a volcano plot between the ORR activity and the adsorption free energy of intermediates on the metal-free materials, similarly to that obtained for metallic catalysts.[178] Liming Dai's group first reported NG as an ORR catalyst in 2010, for which the steady-state catalytic current at the NG electrode was found to be ∼3 times higher than that of Pt/C over a large potential range under alkaline conditions; further, the tolerance to methanol crossover, CO poison effect, and long-term stability were shown to be better than those observed for Pt/C (Figure 6).[97] It was suggested that both pyridine and pyrrolic N in NG are essential for the ORR process. Moreover, a superior ORR performance of NG was also observed by another group.[91,180]

NG@Noble Metals. Ramaprabhu et al. synthesized NG and further used it as a catalyst support for dispersing Pt and Pt–Co alloy nanoparticles, among which Pt_3Co/NG exhibited four times higher power density as compared with commercial Pt/C, caused by an excellent dispersion of nanoparticles on the NG

DOI: 10.1021/acscatal.5b00991
ACS Catal. 2015, 5, 5207−5234

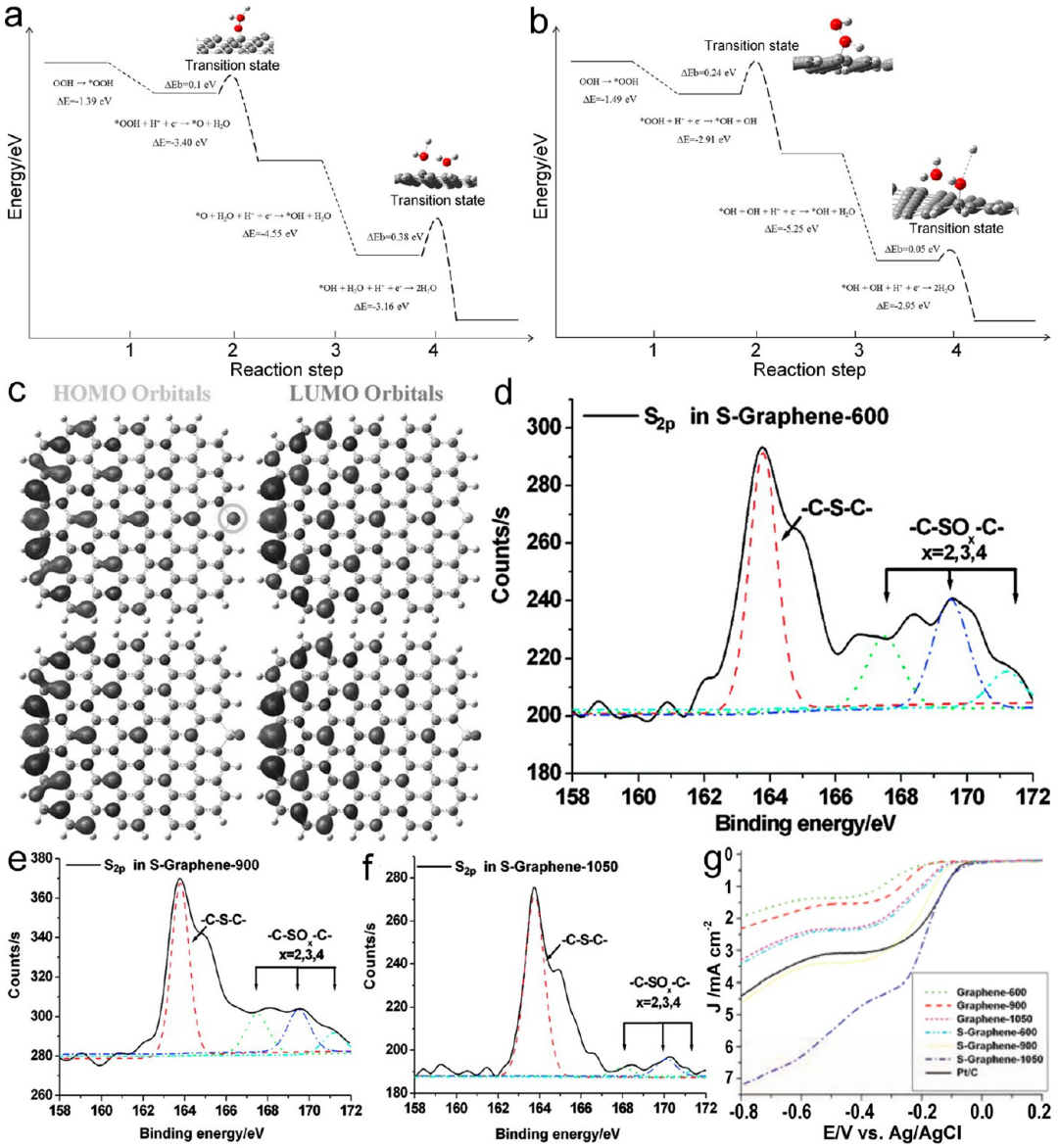

Figure 8. Reaction energy diagram of ORR on (a) S and (b) sulfur oxide graphene. Reproduced with permission from Xia et al.[116] Copyright 2014, American Chemical Society. (c) Highest occupied molecular orbital and lowest unoccupied molecular orbital distributions, the top is S graphene and the below is sulfur oxide graphene. Reproduced with permission from Baek et al.[117] Copyright 2013, Wiley VCH. High-resolution S 2p XPS spectra of (d) S graphene-600, (e) S graphene-900, (f) S graphene-1050; (g) LSVs for various graphenes and a Pt/C catalyst at 1600 rpm on RDE tested in O_2-saturated 0.1 M KOH. Reproduced with permission from Huang et al.[120] Copyright 2012, American Chemical Society.

support, the alloying effect of Pt−Co, and the high electrocatalytic activity of NG.[34] High stability was also observed in Pt/NG and Pt_3Co/NG, suggesting N doping results in strong binding between the nanoparticles and graphene surface, which prevents the detachment of the catalyst from the support and agglomeration during cell operation. Our group achieved an improved ORR performance of Ag/N-rGO nanocomposites, as compared with Ag/graphene, which was assigned to the Ag−N bonding that induced more positive charge on the adjacent C to N. Specifically, it was the pyridinic and pyrrolic N that can be bonded to Ag to get a more negative charge, according to the significantly decreased BE of N 1s XPS spectrum and the obvious Raman enhancement in Ag/N-rGO.[181]

NG@Nonnoble Metal Based Catalysts. It was shown that N dopants in NG can create highly localized states near the Fermi level, which contribute to the strong transition metal bindings that prevent metal aggregation, and favorable adsorption.[182] Müllen's group incorporated Fe nanoparticles into NG, and the hybrid showed nearly 4 e^- process and superior stability in both alkaline (~94%) and acidic (~85%) media.[183]

Despite the stability under alkaline and oxidizing conditions, the low conductivity of metal oxides still limits their ORR activity. Thereby, abundant nonnoble metal oxides were hybridized with conductive NG to improve the ORR performance.[55,177,184−187] Hongjie Dai's group reported a Co_3O_4/NG hybrid in which NG served as nucleation sites for Co_3O_4 to generate a strong coupling between them. A surprisingly high ORR activity was obtained with a more positive ORR peak potentials and higher peak current than those obtained for Co_3O_4/G; namely, an n of ~4.0 at 0.60−0.75 V vs RHE, a small Tafel slope of 42 mV dec^{-1}, and superior durability in 0.1−6 M KOH.[55] Importantly, they proposed that the active reaction sites could be Co oxide species at the interface with NG; therefore, they further

DOI: 10.1021/acscatal.5b00991
ACS Catal. 2015, 5, 5207−5234

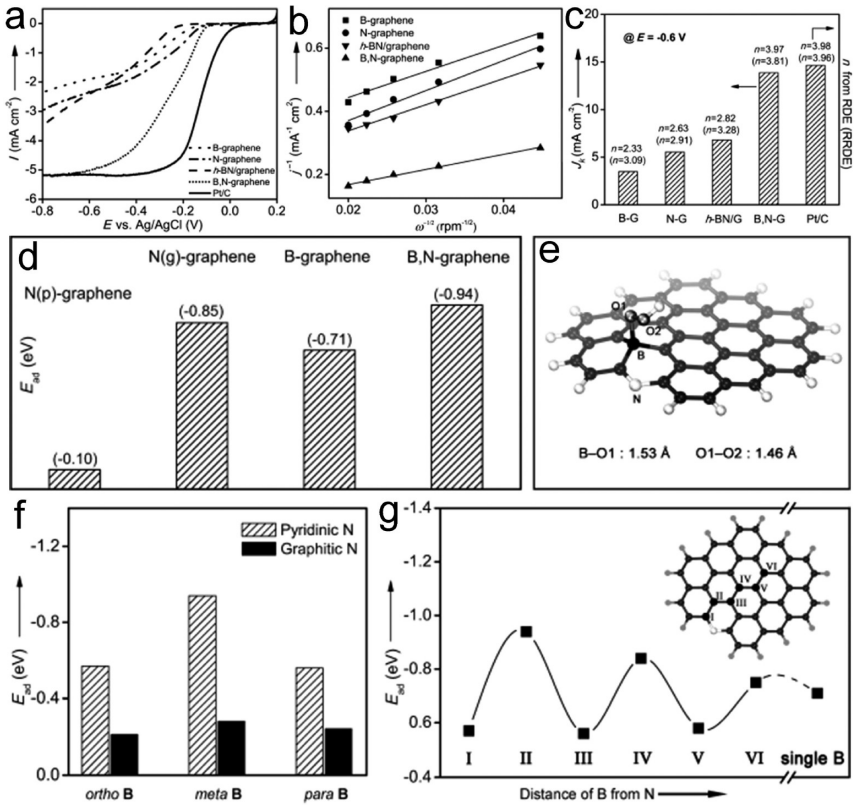

Figure 9. (a) LSVs of various electrocatalysts on a RDE at 1500 rpm in an O_2-saturated 0.1 M KOH (scan rate: 10 mV s^{-1}). (b) K–L plots at −0.6 V. (c) Summary of J_K and n based on the RDE and RRDE data (values in parentheses, G stands for graphene in the x-axis labels). (d) E_{ad} on N- and B-doped graphene. N(p) and N(g) indicate pyridinic and graphitic N bonding, respectively. (e) Optimized configuration of HO_2 adsorbed on B,N-graphene. (f) E_{ad} on various B,N-graphene models with pyridinic or graphitic N groups. (g) E_{ad} on various B,N-graphene models with B active sites as a function of the distance to a pyridinic N atom (sites I–VI as marked in inset). B-graphene with a single B atom was considered as a reference with an infinitely large distance. Reproduced with permission from Qiao et al.[143] Copyright 2013, Wiley VCH.

modified spinel Co_3O_4 with Mn^{3+} substitution to optimize the ORR performance.[177] The resulting $MnCo_2O_4$/NG hybrid exhibited ∼20 mV more positive onset potential and peak potential than those of Co_3O_4/NG and a smaller Tafel slope of 36 mV dec^{-1} owing to the increased catalytic sites. Our group reported a mesoporous Mn_3O_4/NG hybrid with an excellent ORR activity and durability, and for the first time indicated that the ORR activity can be correlated to the shape of nanocrystals, specifically to the exposed crystalline facets.[184,185] The hybrid with Mn_3O_4 ellipsoids (NENG) exhibited the most positive onset potential, −0.13 V; the largest n, 3.81; and highest J_K, 11.69 mA cm^{-2}, at −0.60 V, as compared with those of a cubic (NCNG, 3.70 and 9.38 mA cm^{-2}) or spherical sample (NSNG, 3.64 and 4.70 mA cm^{-2}, Figure 7).[185]

Other types of nonnoble ORR catalysts have also been studied.[188,189] Yu's group reported about ZnSe/NG nanocomposites and proposed that the pyrrolic N atoms played an important role in the enhanced ORR activity under alkaline conditions.[188] Metal nitrides have relatively good stability under acidic conditions and high electrochemical potentials. Hou's group prepared a Fe_xN/NG aerogel hybrid, which exhibited an ORR activity comparable to that of Pt/C. It was found that the large surface area and porosity were responsible for the positive onset potential, and the high density of Fe–N–C sites and small size of Fe_xN particles boosted the charge transfer rate.[189]

3.2.2. BG-Based Catalysts. In addition to NG, it was theoretically found that BG can also promote ORR because it has a lower electronegativity than C, and the positively polarized B atoms attract the negatively polarized O atoms, leading to chemisorption.[190−192] Ferrighi et al. theoretically showed that the formation of bulk borates covalently bonded to graphene (BO_3-G) under oxygen-rich conditions can facilitate the O–O-breaking step in the ORR.[192] Although Wang et al. reported the synthesis of BG with different contents of B and presented that a higher B content in BG increased the electrical resistivity because of the electron acceptor properties of boron; thus, a lower ORR activity was observed in BG with larger B doping.[193]

3.2.3. SG-Based Catalysts. It was confirmed that breaking the electroneutrality of graphitic materials to create charged sites favorable for O_2 adsorption is the key factor in enhancing the ORR activity, regardless of whether the dopants are N, B, or P atoms. The mechanism to promote the ORR on SG is different because of the close electronegativity of S and C. There are four S-doping configurations, whereas the ORR catalytic sites are thought to be C atoms located at the zigzag edges or close to the SO_2 doping and possess highly positive charge density or spin density.[116] The $2e^-$ pathways proceed on the substitutional S atom with high charge density, and 4 e^- transfer takes place on the C atoms with a high positive spin or charge density. According to the calculated energy barrier of ORR reactions on S and oxide S graphene at the zigzag edge (Figure 8a,b), there is no reaction energy barrier for the first OOH molecular adsorbing step and the third electron transfer step. For the second O–O bond breakage step, the energy barrier was 0.1 and 0.24 eV on S graphene and sulfur oxide

DOI: 10.1021/acscatal.5b00991
ACS Catal. 2015, 5, 5207−5234

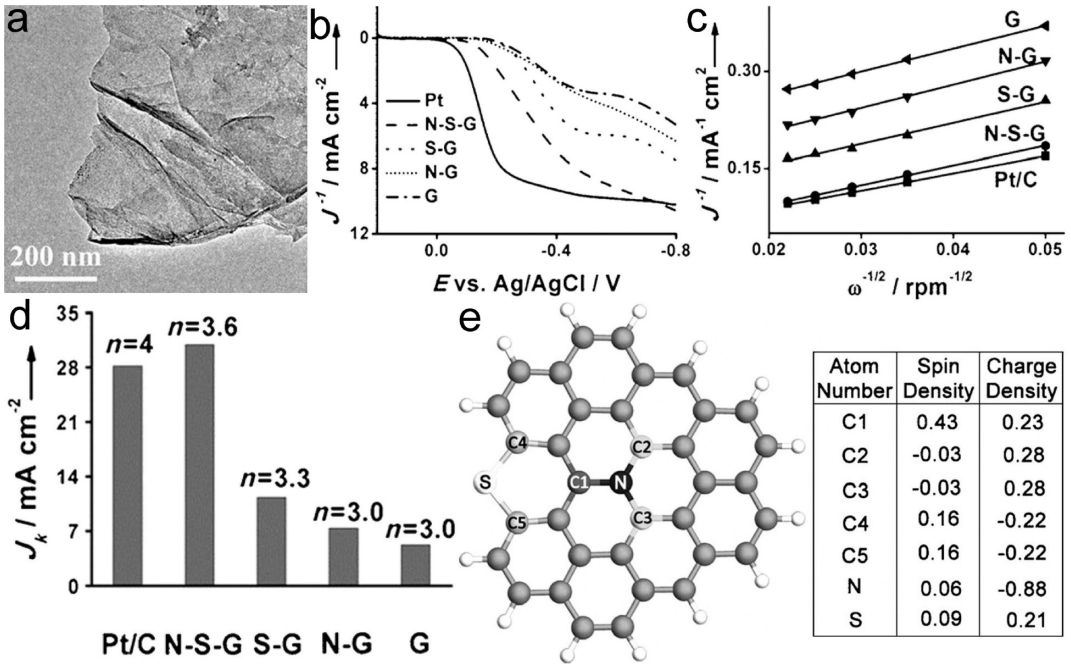

Atom Number	Spin Density	Charge Density
C1	0.43	0.23
C2	-0.03	0.28
C3	-0.03	0.28
C4	0.16	-0.22
C5	0.16	-0.22
N	0.06	-0.88
S	0.09	0.21

Figure 10. (a) TEM image of SNG sheets, (b) LSVs of different samples at 1600 rpm, (c) K–L plots at −0.6 V. (d) J_K as well as the n value at −0.6 V; all samples were tested on RDE in O_2-saturated 0.1 M KOH. (e) Spin and charge density of graphene network (gray) dual-doped by N (black) and S (white). C1 has very high spin density, C2 and C3 have high positive charge density, and C4 and C5 have moderately high positive spin densities. Reproduced with permission from Qiao et al.[151] Copyright 2012, Wiley VCH.

graphene, respectively. In the last H_2O molecule formation step, the reaction barriers are 0.38 and 0.05 eV for the S- and sulfur oxide-graphene. Therefore, it can be concluded that sulfur oxide in SG seems to be better in terms of the energy barriers and the n value for ORR than that of S graphene. Baek's group reported a similar result; specifically, the charge distribution of all S bonding does not change much. There is no spin density on graphene with adsorbed S and a S cluster ring, whereas both charge and spin densities are induced on the graphene with covalently bonded S and oxidized S (Figure 8c).[117] However, Huang's group proposed that the C–S bonding is an important catalytic active site for the ORR; therefore, the activity increased with increasing –C–S–C– content and decreasing sulfur oxide content, although the overall S content was decreasing (Figure 8d–g).[120]

In addition, Park et al. found that SG showed higher ORR activity with a large J_K and durability, and NG improved the onset potential.[194] Chen et al. synthesized SG and adopted it as a support for Pt catalysts; consequently, the strengthened interactions between Pt and SG could lead to a catalyst–support tethering effect and a negatively shifted d-band center of Pt atoms, which is essential for the enhanced ORR.[195] 3D SG networks that displayed good ORR performance due to the S-doping enhanced activity and the 3D porous structure assuring facile mass transport and ionic diffusion were also fabricated.[126,196,197]

3.2.4. PG-Based Catalysts. The P atoms and their neighboring C atoms are thought to be the preferred adsorption sites and the active centers for ORR.[198] The ORR around P dopants in PG may first proceed by $2e^-$ process to form the OOH intermediate, followed by $4e^-$ process to break the O–O bond of OOH. The second OH hydrogenation to H_2O is the rate-determining step (RDS) because of its largest reaction barrier of 0.88 eV. The P dopant could tune the electronic structure of graphene by donating 0.21 e^- to the adjacent C atoms, and it would further diminish the electron (0.34 e^-) when adsorption of O_2, O, H_2O, OH, and OOH happen, suggesting that the electrons transferred to adsorbates are mainly from P dopants. Interestingly, the electrons gained by O when adsorbed on PG exceed those lost by P, indicating the P atom can act as a bridge for the electron transfer from C to the adsorbates. Li et al. confirmed the above ORR mechanism experimentally; the obtained PG displayed a competitive ORR performance with an onset potential of 23.5 mV only (negatively shifted from that of Pt/C), n values higher than 3.6, and an extraordinary stability with 3.57% current loss after 16 000 s.[135] Furthermore, Yu's group investigated the synergistic effect between P dopants and metal centers (Fe) in graphene materials for ORR, which generates the electrochemically active Fe–P species.[199] Interestingly, PG becomes active in acidic medium as a result of the excellent blend of Fe and P functionalization and improved active surface area.

3.2.5. BNG-Based Catalysts. The formation of B and N as separated states in BNG would facilitate ORR, whereas the formation of BN domains may show the graphite-like ORR activity.[143,144,146] Our group conducted a detailed investigation on the *h*-BN-free BNG that exhibited a positive ORR onset potential, showing a nearly perfect 4 e^- pathway, as well as J_K of 13.87 mA cm^{-2} that surpasses the summed value of BG (3.48 mA cm^{-2}) or NG (5.54 mA cm^{-2}; all the samples were tested using the same electrochemical system under the same conditions; Figure 9a–c) because of the synergistic effect between B and N dopants.[143,144,147] The BNG has a higher energy of HO_2 adsorption (E_{ad}) than graphitic NG, BG, and pyridinic NG; its ORR active sites are the 3-fold-coordinated B dopant in B–C–N heteroring in which the C 2p orbital located between the N and B dopants is first polarized by N and then able to donate extra electrons to an adjacent B atom (Figure 9d,e). Unexpectedly, only the pyridinic N can boost HO_2

DOI: 10.1021/acscatal.5b00991
ACS Catal. 2015, 5, 5207–5234

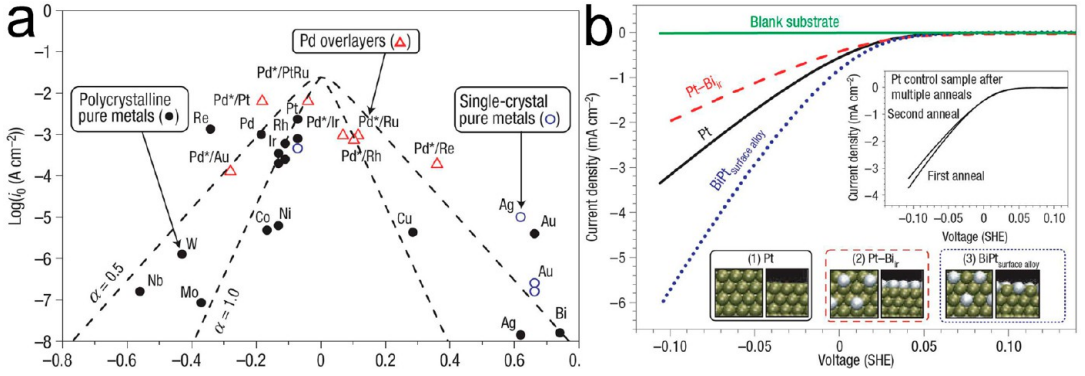

Figure 11. (a) Volcano plot for the HER for various pure metals and metal overlayers (denoted by Pd*/substrate). ΔG_{H^*} values are calculated at 1 bar of H_2 (298 K) and at a surface hydrogen coverage of either 1/4 or 1/3 monolayer. The two curved lines correspond to the activity predictions of the simple mean-field, microkinetic models, assuming transfer coefficients (α) of 0.5 and 1.0, respectively. (b) Hydrogen evolution after each stage of BiPt surface alloy synthesis on a fluorine-doped tin-oxide substrate. (1) Pt film after deposition and annealing, (2) immediately after Bi_{upd}, and (3) after second annealing to form the BiPt surface alloy. The inset represents a control sample Pt film without Biafter first and second annealing. Current densities are normalized to the surface area of the initial, pure Pt sample, determined by H_{upd}. Reproduced with permission from Nørskov et al.[38] Copyright 2006, Nature.

adsorption on the active B atoms, with the B atom meta to a pyridinic N atom showing the highest E_{ad} value, whereas an ortho B atom directly bonded to N as BN having the lowest activity owing to the lack of the C bridge (Figure 9f). Furthermore, the strength of the synergistic effect decreases gradually as the distance between the B and pyridinic N dopants increases (Figure 9g). Nevertheless, Lee et al. reported the origin of the ORR catalytic activity could be the insertion of B and N atoms as BCO_2 and pyrrolic N.[142] Tour's group synthesized a B and N codoped GQD/graphene hybrid, which combined the advantages of both components, such as abundant edges and doping sites, high electrical conductivity and high surface area, leading to a higher ORR activity than that of Pt/C in alkaline media.[200]

3.2.6. SNG-Based Catalysts. We reported a mesoporous SNG as the ORR catalyst (Figure 10a), which displayed a positive onset potential of −0.06 V vs Ag/AgCl, an n value between 3.3 and 3.6, and a high J_K exceeding that of Pt/C at −0.6 V (the as-prepared samples and commercial Pt/C were measured in the same electrochemical system under the same conditions, Figure 10b–d).[151] It was found that when S and N were doped into the graphene matrix simultaneously, the maximum spin density was raised to 0.43 (C1), which should be responsible for the elevated ORR activity of SNG and the synergistic ORR enhancement resulting from the asymmetrical spin and charge densities, leading to a large number of carbon atom active sites (C1–C5, Figure 10e). The enhancement of the synergistic effect for ORR by S and N dual doping has also been discussed by other groups.[149,152,154] Zhang et al. revealed that the doping of N/S heteroatoms into the graphene matrix with different numbers of valence electrons synergistically modulates the electronic properties of host graphene and introduces additional states, such as electron-acceptor or -donor states, thus creating favorite active sites for ORR.[154]

4. HER ELECTROCATALYSTS

The HER's total equation and detailed pathways are summarized as follows:[57,201] In acidic media, the first step of HER is adsorption of hydrogen on the electrode surface by transferring a proton from the electrolyte combined with one electron from the electrode (Volmer reaction). For the second step, there are two possibilities: one is the Heyrovsky reaction in which the adsorbed hydrogen atom (H*) reacts with one electron and one proton to form one H_2 molecule; the other one is the Tafel reaction in which two adjacent H* combine to form one H_2 molecule. The HER reactions in alkaline media require an additional water dissociation step, which would introduce an additional energy barrier affecting the whole reaction rate. The determination of the RDS can be simply discerned by the Tafel slope value from the LSVs through the Tafel equation ($\eta = b \log j + a$, where j is the current density and b is the Tafel slope), which is an inherent property of the catalyst. By extrapolation, the Tafel plots at low overpotentials to the j axis, the exchange current density (defined as j_0) can be obtained. For example, in the case of Pt with nearly 100% hydrogen coverage, the Tafel slope at low overpotentials is usually measured as 30 mV dec^{-1}; therefore, the Volmer–Tafel mechanism, eqs 12 and 14, is determined, and the recombination Tafel step is the RDS.

In acidic media:

$$H^+ + e^- + * \rightarrow H^* \quad \text{(Volmer)} \tag{12}$$

$$b = \frac{2.3RT}{\alpha F} \approx 120 \text{ mV dec}^{-1}$$

$$H^+ + e^- + H^* \rightarrow H_2 \quad \text{(Heyrovsky)} \tag{13}$$

$$b = \frac{2.3RT}{(1+\alpha)F} \approx 40 \text{ mV dec}^{-1}$$

or

$$2H^* \rightarrow H_2 \quad \text{(Tafel)} \tag{14}$$

$$b = \frac{2.3RT}{2F} \approx 30 \text{ mV dec}^{-1}$$

In alkaline media:

$$H_2O + e^- \rightarrow H^* + OH^- \quad \text{(Volmer)} \tag{15}$$

$$H_2O + e^- + H^* \rightarrow H_2 + OH^- \quad \text{(Heyrovsky)} \tag{16}$$

or

$$2H^* \rightarrow H_2 \quad \text{(Tafel)} \tag{17}$$

DOI: 10.1021/acscatal.5b00991
ACS Catal. 2015, 5, 5207–5234

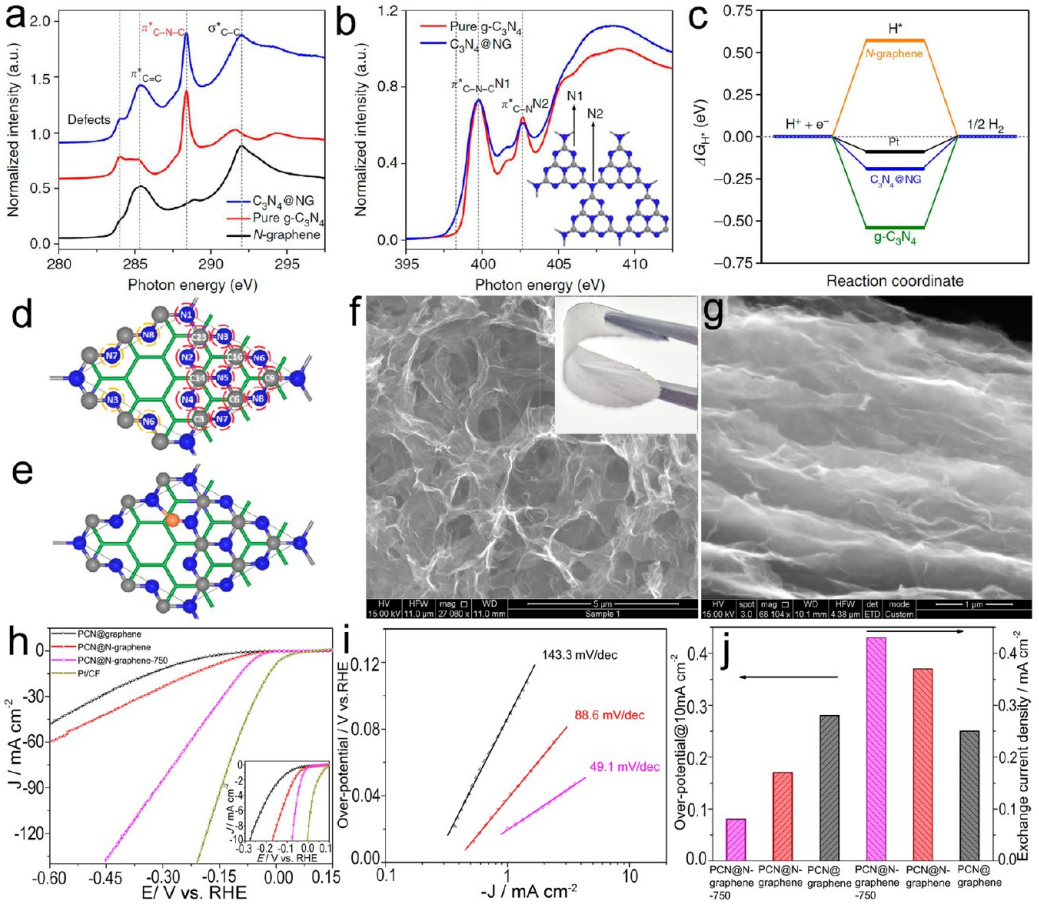

Figure 12. C_3N_4@NG: (a, b) C and N K-edge near-edge X-ray absorption fine structure (NEXAFS) spectra of different catalysts. An inset illustrating two types of N species in g-C_3N_4; blue designates N; gray designates C atoms. A weaker shoulder on the spectrum of C_3N_4@NG at 398.3 eV is assigned to the π^*_{C-N} resonance of the N heteroatom in NG. (c) The calculated free-energy diagram of HER at the equilibrium potential for three metal-free catalysts and Pt reference. (d) Possible H* adsorption sites (highlighted by red circles) on C_3N_4@NG; yellow circles denote the equivalent atoms. The N-doping site on graphene is beneath C23. (e) The most stable H* adsorption pattern on N2. Green designates C on graphene, gray designates C on g-C_3N_4, and blue designates N on g-C_3N_4. Reproduced with permission from Qiao et al.[240] Copyright 2014, Nature. PCN@N-graphene film: (f, g) Scanning electron microscope images of the inside structure and cross-sectional view; inset is its photograph. (h) LSVs; inset shows LSVs with current density below 10 mA cm^{-2}). (i) Tafel plots at low overpotentials. (j) Overpotential at 10 mA cm^{-2} vs RHE (left) and j_0 (right). All the tests were conducted in N_2-saturated 0.5 M H_2SO_4. Adapted with permission from Qiao et al.[50] Copyright 2015, American Chemical Society.

where R is the ideal gas constant, T is the absolute temperature, $\alpha \approx 0.5$ is the symmetry coefficient, and F is the Faraday constant.

4.1. Traditional HER Catalysts. Metals and their alloys have been extensively investigated as traditional HER electrocatalysts.[38,201−206] Nørskov's group reported the HER activity for metals and over 700 binary alloys and presented a volcano plot using experimentally measured log j_0 against the DFT calculated Gibbs energy of hydrogen adsorption (ΔG_{H^*}, Figure 11a).[38,207] In particular, the optimum value should be around $\Delta G_{H^*} = 0$, and BiPt was found to have an activity comparable to or even better than pure Pt (Figure 11b). On the basis of the Brewer−Engel theory, Jakšić indicated that the electronic configuration of alloys can determine their HER activity.[208] According to this study, whenever the left-half transition metals that have empty or half-filled d orbitals are alloyed with the right-half transition metals that have paired d electrons, there is an enhanced synergy in HER electrocatalysis. As result, the highest electrocatalytic activity is observed for the d metal composite with improved d orbital overlap in intermetallic phases, such as $MoCo_3$, WNi_3, $MoNi_3$, $LaNi_5$. In addition, a pronounced structure sensitivity of the HER activity has been demonstrated.[204−206] Markovic's group demonstrated that the Pt(110) displayed ∼10 times higher ORR activity than the (100) or (111) faces at 275 K, which can be attributed to the structure-sensitive adsorption of underpotentially deposited hydrogen (H_{upd}) and hydroxyl species (OH_{ad}) and the effect these species have on the formation of the electroactive intermediate, overpotential deposited hydrogen (H_{opd}).[205] Obvious differences in HER occurring in acidic and alkaline media were noticed, and alkaline HER is usually promoted by Ni and their alloys.[44,209−211] Lasia et al. demonstrated the Volmer−Heyrovsky mechanism on both polycrystalline Ni and NiAl alloy electrodes in alkaline media, which are very active despite large Tafel slopes.[210,211]

Molecular catalysts have been applied to catalyze HER.[212,213] Goff and colleagues showed that the covalent attachment of a nickel bisdiphosphine-based mimic of the active site of hydrogenase enzymes onto MWCNTs results in high HER activity and exceptional stability in acid.[212] Bhugun et al. have found that iron(0) porphyrins are efficient and persistent HER catalysts that bear some resemblance to complexes in which a

DOI: 10.1021/acscatal.5b00991
ACS Catal. 2015, 5, 5207−5234

substantial electron density at the Fe atom is transferred from S-containing ligands.[213]

Metal oxides have also been studied as HER catalysts.[214−217] Gong et al. reported nanoscale nickel oxide/nickel heterostructures formed on the CNT sidewalls as effective HER electrocatalysts with activity similar to that of Pt, in which the metal ion-CNT interactions impede complete reduction and Ostwald ripening of nickel species into a less active Ni phase.[216] It was reported that metal carbides exhibit HER activities similar to those of Pt group metals, yet they are more abundant and less expensive. Hunt et al. synthesized metal-terminated metal carbide nanoparticles in the 1−4 nm range with tunable size, composition, and crystal phase, among which WC and $Mo_xW_{1-x}C$ nanoparticles are highly active and stable HER catalysts with activities of ∼100-fold higher than that of commercial WC and similar to that of Pt-based catalysts.[218] Very recently, metal phosphides were extensively investigated as HER catalysts.[219,220] Sun's group prepared a closely interconnected network of MoP nanoparticles with a Tafel slope of 54 mV dec^{-1} and j_0 of 0.086 mA cm^{-2}.[221] Jaramillo and colleagues obtained a molybdenum phosphosulfide (MoP|S) catalyst with superb activity and stability for HER in acidic media, which represents a more uncommon mixed-anion catalyst with synergistic effects between S and P that is more active than undoped sulfide or phosphide.[220]

Layered transition metal dichalcogens (TMDCs) have been found to be especially active in HER electrocatalysis. Although the bulk MoS_2 exhibits poor HER activity, a nanoparticulate MoS_2 is a promising system because of the abundant active edges.[45,222] It was shown that the HER activity of TMDCs can be further promoted by incorporating other transition metals, such as Co, Ni, etc.[223,224] Chorkendorff's group incorporated Co into MoS_2 and WS_2 to promote their activity toward HER. In this case, the cobalt-promoted MoS_2 (Co−MoS_2) was shown to be better than cobalt-promoted WS_2 (Co−WS_2) because the former have active sites on both edges and therefore feature a higher total number of active sites.[224] Interestingly, 2D TMDCs nanolayers have displayed drastically improved HER activity owing to a significant increase in the number of edge active sites and specific surface area in addition to the different band structure and chemical terminations of 2D nanolayers.[225−228] Metallic 1T-MoS_2/WS_2 can overcome the inherently low electrical transport property of 2H-TMDCs, and exhibit metallic conductivity and proliferated density of active sites caused by the strained lattice distortion, which improves the HER kinetics and activity.[229,230] Because of the instability of the isolated 2D materials, Hongjie Dai's group developed a MoS_2/rGO hybrid with high HER performance, consisting of a few-layer MoS_2 with abundant active edges stacked onto conductive graphene.[231] Moreover, Cui's group prepared 3D HER electrodes composed of $CoSe_2$ nanoparticles grown on carbon fiber paper, which exhibited excellent catalytic activity and exceptional durability in an acidic electrolyte.[232]

4.2. Heteroatom-Doped Graphene Based Catalysts.

The widely applied metallic catalysts for HER usually suffer inherent corrosion and oxidation susceptibility under acidic conditions. Therefore, nonmetal HER catalysts have been widely investigated.[233−237] Misra et al. used a vertical array of CNTs to promote HER by taking advantage of the CNT conductivity and utilizing their top surfaces as an electrode.[233] Qu's group fabricated 3D networks from 1D g-C_3N_4 nanoribbons on 2D graphene sheets, which provides a large accessible surface area, multielectron transport channel, and short diffusion distance for efficient charge separation and transfer in HER.[235] In addition, N-doped hexagonal carbons exhibited high HER activities stemming from the intrinsic electrocatalytic property of hexagonal nanodiamond, rapid charge transfer, and abundance of active sites after N-doping.[238] Herein, we present a brief overview of the heteroatom-doped graphene-based HER catalysts.

4.2.1. Monodoped Graphene. Sathe et al. reported BG as an efficient HER electrocatalyst, with a Tafel slope of ∼99 mV dec^{-1}, j_0 of 1.4×10^{-3} mA cm^{-2}, good durability, and only negligible loss of the cathodic current in 0.5 M H_2SO_4 solution.[239]

Our group coupled g-C_3N_4 with NG to produce a metal-free hybrid catalyst (Figure 12a−e) that showed a small overpotential of ∼240 mV to achieve a 10 mA cm^{-2} current density, a small Tafel slope of 51.5 mV dec^{-1}, and a j_0 of 3.5×10^{-7} A cm^{-2}.[240] The interfacial covalent bonds between g-C_3N_4 and NG layers afforded a strong molecular framework, guaranteeing a robust stability in both acidic and alkaline solutions. A largely negative ΔG_{H^*} of −0.54 eV for g-C_3N_4 suggests that chemical adsorption of H* on its surface is too strong; in contrast, a largely positive ΔG_{H^*} of 0.57 for NG indicates very weak H* adsorption; therefore, both pure g-C_3N_4 and NG are unfavorable for HER. However, C_3N_4@NG hybrid showed the smallest $|\Delta G_{H^*}|$ of 0.19 eV, indicating a mediated adsorption−desorption behavior. A synergistic effect for this hybrid catalyst was identified in which g-C_3N_4 provides highly active hydrogen adsorption sites by forming C_2N_3H heterorings via one H* bonding with two pyridinic N present in one tri-s-triazine periodic unit, while NG facilitates the electron transfer for the proton reduction. In addition, we modified the electrode architecture by constructing a 3D film that can be directly used as an HER catalyst electrode without the membrane electrode assembly, featuring flexibility, highly exposed active sites in C_3N_4 nanolayers, facile mass transport due to the hierarchical porous structure, and a strong synergistic effect between 2D C_3N_4 and the doped graphene sheets.[50] The as-prepared porous 2D C_3N_4 and NG hybrid film (PCN@N-graphene film) displayed a small overpotential (80 mV vs RHE @ 10 mA cm^{-2}) and Tafel slope of 49.1 mV dec^{-1}, a high J_0 of 0.43 mA cm^{-2}, and remarkable durability (seldom activity loss >5000 cycles), outperforming many metal catalysts (Figure 12f−j).

In addition, we incorporated molecular clusters (MoS_x) into a 3D NG hydrogel film, which showed a very good HER performance with dual active sites from both pyridinic and pyrrolic N in NG and defects and edges of MoS_x.[241] Hou et al. prepared a hybrid consisting of NG/Co embedded in porous carbon polyhedron (N/Co-doped PCP/NG) that exhibited an excellent HER performance offering positive onset overpotential of 58 mV and a stable current density of 10 mA cm^{-2} at 229 mV in acid media, also with the dual active site mechanism resulting from remarkable features of the porous carbon structure, N/Co-doping effect and good contact between components.[242]

4.2.2. Double-Doped Graphene. Chen's group reported SNG with a high density of both dopants and structural defects, which shows an outstanding HER activity with a Tafel slope of 80.5 mV dec^{-1} and overpotential of −0.28 V at 10 mA cm^{-2}.[150] It was suggested that C defects alone in graphene are not catalytically active for HER, whereas the coupling of S and N dopants with geometric defects in graphene lattice produces a synergistic effect that allows precise tuning of ΔG_{H^*} to achieve an outstanding HER activity. The SNG model with one C

DOI: 10.1021/acscatal.5b00991
ACS Catal. 2015, 5, 5207−5234

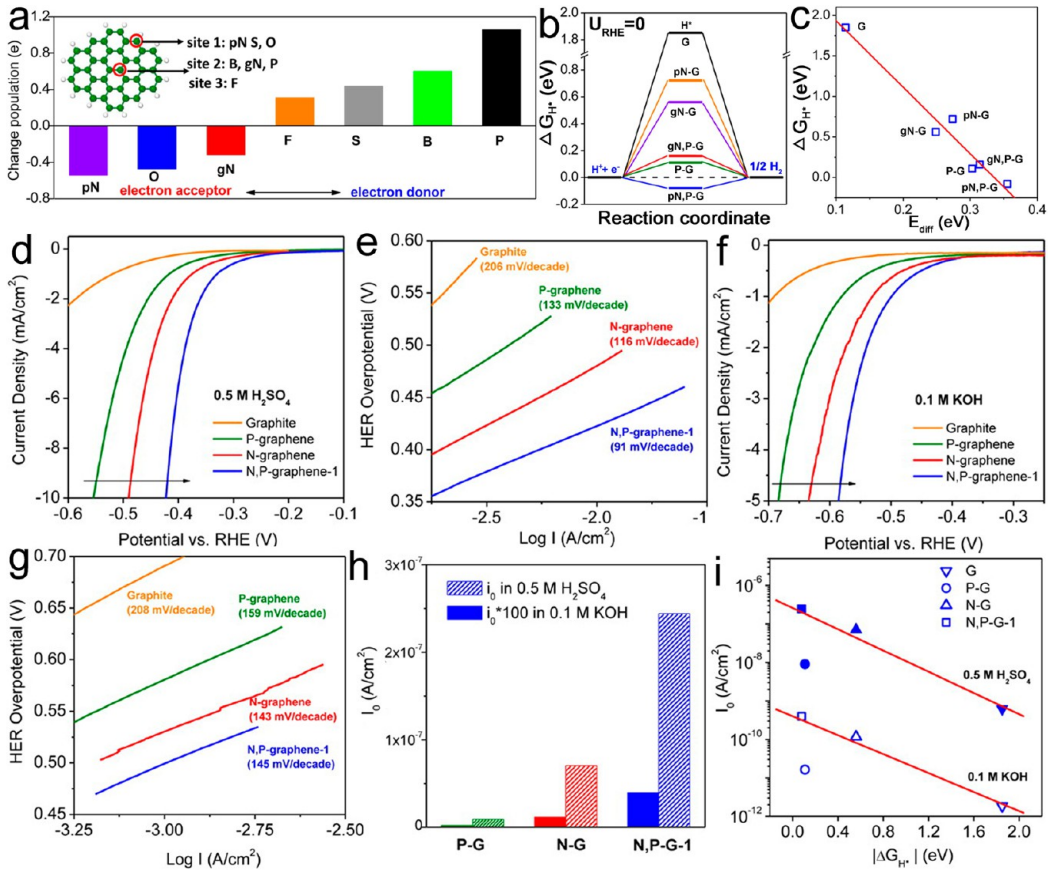

Figure 13. (a) Natural bond orbital population analysis of six different nonmetallic heteroatoms in graphene matrix. pN and gN designate pyridinic and graphitic type of N, respectively. The inset shows the proposed doping sites for different elements. Sites 1 and 2 are the edge and center in-plane sites, respectively, and site 3 is an out-of-plane center site in graphene. (b) The calculated ΔG_{H^*} diagram for HER at the equilibrium potential (U_{RHE} = 0 V) for N- and P-doped graphene models. (c) Relationship between ΔG_{H^*} and E_{diff} for various models. (d–g) LSVs and the corresponding Tafel plots of N- and P-doped graphene electrocatalysts in (d, e) 0.5 M H_2SO_4 (pH = 0) and (f, g) 0.1 M KOH (pH = 13). (h) Comparison of calculated exchange current density i_0 values for N- and P-doped graphenes in 0.5 M H_2SO_4 (patterned bars) and 0.1 M KOH (solid bars) solutions, (i) Relationships between i_0 and ΔG_{H^*} for N- and P-doped graphenes. Reproduced with permission from Qiao et al.[243] Copyright 2014. American Chemical Society.

defect near the S doping site (−C−S−C− or −C═S−) in the vicinity of graphitic N has the smallest ΔG_{H^*} value of 0.12 eV, comparable to that of a Pt catalyst (0.09 eV). Moreover, the induced positive and negative charge density distribution as well as the negatively shifted Fermi level (0.6 eV above the Dirac point) could facilitate HER.

Importantly, our group designed double-doped graphene by using a couple of the dopants with the most noticeable differences in the charge population (i.e., N and P), to maximally activate the adjacent C atom and consequently enhance the HER activity (Figure 13a).[243] By DFT calculations, the pyridinic N and P double-doped model (pN,P-G, meta-type pN and P in the heteroring) has the lowest ΔG_{H^*} value of −0.08 eV, indicating its highest HER activity due to the most favorable hydrogen adsorption−desorption property (Figure 13b). Using the molecular orbital theory, the lowest ΔG_{H^*} value originates from the highest E_{diff} (defined as the difference between the lowest valence orbital energy of the C active center and the highest valence orbital energy of the graphene cluster) in the pN,P-G cluster (Figure 13c). As expected, the PNG displayed the highest HER activity, with an overpotential of ∼420 mV, to achieve 10 mA cm^{-2} current density and the lowest Tafel slope of 91 mV dec^{-1} in 0.5 M H_2SO_4 solution (Figure 13d,e). In addition, a synergistic enhanced doping effect of N and P was observed in the HER activity. Interestingly, the HER activities of all catalysts in alkaline solutions were lower than those in acidic solutions with the activity following the same trend (Figure 13d–i). The difference may arise from the aforementioned different HER mechanisms in the two different electrolytes. For example, there is an additional water dissociation step in the alkaline solution, and graphene-based catalysts are unfavorable to facilitate this step that results in a relatively high energy barrier in the whole HER process.

5. OER ELECTROCATALYSTS

OER may be performed under basic or acidic and neutral solutions as follows:[62,244,245]

in alkaline solutions

$$4OH^- \rightarrow 2H_2O + O_2 + 4e^- \quad (18)$$

in acidic or neutral solutions

$$2H_2O \rightarrow 4H^+ + O_2 + 4e^- \quad (19)$$

It was shown that the efficiency of oxygen-evolving electrocatalysts is determined to a large extent by the strength of the binding of the reaction intermediates (HO*, O*, and HOO*) to the electrode surface.[62] The performance of

DOI: 10.1021/acscatal.5b00991
ACS Catal. 2015, 5, 5207−5234

electrocatalysts can be evaluated by comparing their activities, stability, and faradic efficiencies.[245] Specifically, the activity is determined by the overpotential required to achieve a current density of 10 mA cm^{-2} per geometrical area, which is approximately the current density expected for a 10% efficient solar-to-fuels conversion device. The stability test is performed by operating a device for an extended period of time. The faradic efficiency of an OER catalyst is determined by quantifying the amount of dissolved generated O_2 and dividing it by the amount of expected O_2 based on the charge passed during electrolysis.

5.1. Homogeneous Catalysts for OER. In nature, OER is efficiently accomplished by photosystem II (PSII) containing $CaMn_4O_x$ clusters. Inspired by PSII, various artificial molecular clusters have been designed and synthesized. Early studies of homogeneous catalysts include precious-metal-based clusters (such as a Ru-based complex).[75] however, the use of precious metals is costly, and the majority of homogeneous catalysts are still thermodynamically unstable with respect to the oxidative degradation. As a consequence, a number of homogeneous catalysts based on earth-abundant elements (Co,[58] Cu,[73] Fe,[74] etc.) with enhanced stability have been reported. On the other hand, the catalytic activity of homogeneous catalysts has also been improved by introducing another metal (such as Ru), which often features an increased amount of catalytic centers.[76] Recently, two strategies have been reported to integrate homogeneous and heterogeneous catalysts to achieve both high stability and activity: one is the immobilization of molecular clusters on the heterogeneous surfaces, such as polyoxometalate on carbon nanotubes,[78] and the other method is the transformation of homogeneous clusters into heterogeneous materials, such as electrodeposition of $[Ni(en)_3]Cl_2$ (en =1,2-diaminoethane) on nickel oxide.[77]

5.2. Heterogeneous Catalysts for OER. Volcano plots play an important role in electrocatalysis, which can correlate the intrinsic surface adsorption properties and electronic structure of a catalyst with its apparent catalytic activity.[246] This relationship can be illustrated by a single descriptor, as shown in Figure 14.[247] Both theoretical and experimental studies confirmed the high activities of noble metals for electrocatalytic OER, in which the overpotential sequence for OER in acidic solutions is Ru < Ir < Pd < Rh < Pt.[248] RuO_2-based materials are the most active electrocatalysts,[60] but they exhibit weak stability under oxidation conditions because of the formation of solvable ruthenium tetroxide (RuO_4) under high anodic potential (>1.4 V).[61] As an alternative to Ru, iridium oxide (IrO_2) that possesses an increased stability up to 2.0 V anodic potential has received enormous interest, despite its slightly lower activity.[63] To achieve an enhanced activity for OER, various Ru and Ir alloys and oxides have been studied recently, for example, Ru−Ir Pyrochlores,[65] $IrNiO_x$ core/shell particles, etc.[64]

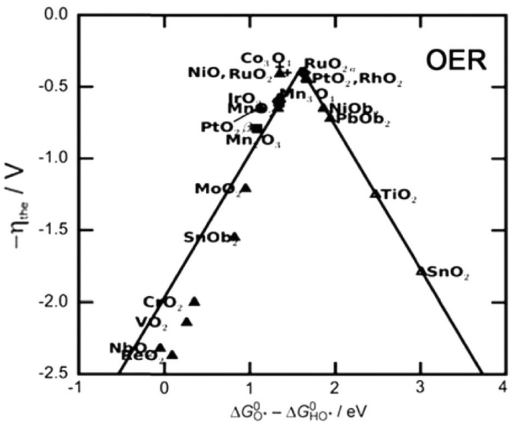

Figure 14. Volcano plots for different surfaces. OER activity trends for oxides as a function of the standard free energy of the $\Delta G_{HO^*}-\Delta G_{O^*}$ step. The activity is expressed by the value of overpotential to achieve a certain value of current density. Reproduced with permission from Nørskov et al.[247] Copyright 2011, Wiley VCH.

Because of the scarcity and high cost of noble metals, tremendous efforts have been devoted to the development of nonnoble metal catalysts for OER in alkaline and neutral electrolytes. The mostly studied and still popular electrocatalysts are Ni-, Co-, and Mn-based oxides (both free-standing and supported on carbon or other metals). Markovic et al. compared the overall catalytic activities for various OER catalysts in alkaline solutions as a function of OH−M (M = transition metal oxides) bonding strength, which exhibits the trends in reactivity (Mn < Fe < Co < Ni).[249] Interestingly, these trends seem to be independent of the source of OH in the supporting electrolyte. In another work, Nakamura and his co-workers developed Mn oxides-based electrocatalysts by coordinating amine groups of poly(allylamine hydrochloride) with the surface Mn sites of MnO_2 electrodes.[250] They found that the formation of N−Mn bonds can effectively stabilize the Mn^{3+} species, resulting in a 500 mV negative shift of the onset potential for OER at neutral pH. In addition to crystalline metal oxides, the Dau[251] and Berlinguette[252] groups have prepared the amorphous metal oxides (such as Mn oxides and $Fe_{100-y-z}Co_yNi_zO_x$), which can exhibit high activity comparable even to that of noble metal catalysts used in commercial electrolysis. Moreover, a number of mixed transition metal oxides in the form of perovskites,[57] double perovskites,[253] and spinels[254] have also been reported to achieve the enhanced catalytic activities.

Beyond oxides, transition metal-based hybrids consisting of hydroxides, phosphates, boron compounds, nitrates, etc. have also been extensively studied. For example, the Müller[255] and Hu[256] groups prepared NiFe hydroxide nanosheets by using pulsed-laser ablation and liquid exfoliation methods. A significant increase in the OER activity was observed for these nanosheets in comparison with its bulk counterpart due to the electrochemical surface area and the number of active edge sites. Nocera et al.[68] prepared cobalt phosphate by electrodeposition of cobalt-containing salts in phosphate solution. The study of OER on this catalyst electrode under benign conditions (pH = 7, 1 atm and room temperature) showed an overpotential of 0.28 V at the current density of 1 mA cm^{-2}. On the other hand, Xie et al. reported the fabrication of metallic Ni_3N nanosheets by a facile hydrothermal method, followed by thermal annealing in an ammonia atmosphere. Benefitting from enhanced electrical conductivity associated with metallic behavior and atomically disordered structure, the Ni_3N nanosheets showed an intrinsically improved OER activity as compared with that of bulk Ni_3N and NiO nanosheets.

Very recently, nonmetal electrocatalysts based on carbon and organic frameworks have received enormous interest due to their low cost, high stability, and environmental friendliness.[56,69,257−259] The first reported nonmetal electrocatalyst for OER is an organic compound, *N*(5)-ethylflavinium ion,[56]

DOI: 10.1021/acscatal.5b00991
ACS Catal. 2015, 5, 5207−5234

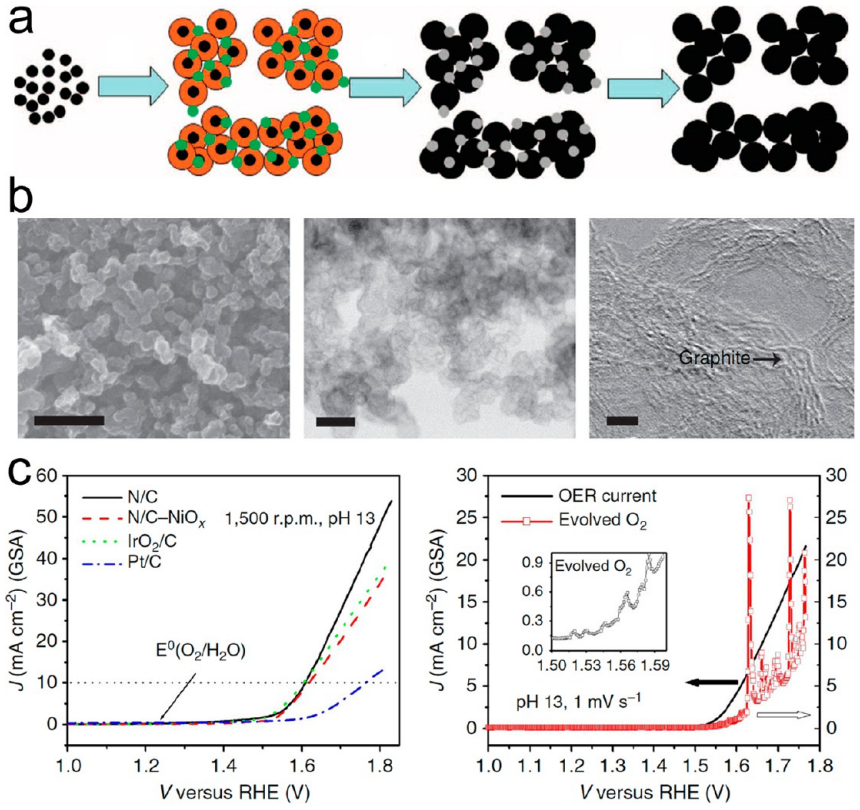

Figure 15. Preparation procedure (a), morphology (b), and OER catalytic activity (c) of nitrogen-doped graphite electrocatalyst. Reproduced with permission from Hashimoto et al.[69] Copyright 2013, Nature.

which can mediate oxygen evolution via a four-electron transfer reaction. Nevertheless, a much higher overpotential is required for this electrocatalyst (0.73 V vs RHE, pH 2) as compared with the existing transition metal-based catalysts (0.3−0.5 V vs RHE), which is presumably due to its low electrical conductivity and impeded charge transfer.

Therefore, Hashimoto et al. prepared a conductive nitrogen-doped graphite electrocatalyst (Figure 15) that can generate a current density of 10 mA cm^{-2} at an overpotential of 0.38 V.[69] The electrochemical and physical studies indicate that the catalytic centers for OER are the pyridinic N or graphitic N type active sites. Recently, we and other groups have demonstrated that nanostructured carbons are promising candidates for nonmetal OER electrocatalysts, such as g-C_3N_4;[258] heteroatom-doped graphenes;[260] 3D N, P-doped porous carbons;[259] and surface-oxidized carbon nanotubes.[257] These nanostructured materials can be obtained with the high surface area and well-developed suitable porosity needed for transport of reactants and products as well as exposed active centers desirable for enhanced kinetics, assuring a current density of 10 mA cm^{-2} at an overpotential of about 0.3 V.

5.3. Heteroatom-Doped Graphene for OER. Different from the graphene-based catalysts for ORR, which have been widely investigated and shown to be competitive, the studies of heteroatom-doped graphene materials for OER have just started. In many studies, doped graphene has been used primarily as a high-surface-area conductive support for anchoring transition metal materials, such as Co_3O_4 nanoparticles,[55] Co embedded carbons,[242] the Co/Co_3O_4 hybrid,[71] and copper nanoclusters.[261] A dual-active-center mechanism was proposed for these hybrid systems, that is, the metal species as the main contributor and heteroatom doped-carbon (such as C−N) species as additional centers for OER. It was proven that the performance of hybrid materials strongly correlates to the crystal structure of the metal oxides nanoparticles. For example, low surface energy exposed facets of Co_3O_4 nanoparticles showed an improved activity as compared with other structured counterparts.[262] A suitable integration of heteroatom-doped graphene with transition metal oxides can create a significant number of available catalytic sites and ensure an efficient charge transport, which can result in enhanced catalytic activity toward OER.

In this area of research, our group has recently reported a series of 3D NG frameworks, such as graphene papers and hydrogels, as new-generation scaffolds to confine transition metal nanoparticles.[70,260,263] For example, nickel nanoparticles have been directly grown inside the NG films via a heterogeneous reaction process (Figure 16). The as-formed 3D hybrid exhibited remarkable structural properties for favorable electrocatalysis. First, by blending Ni nanoparticles with NG sheets, Ni may act as a spacer to inhibit the restacking of graphene sheets and to generate large meso/macropores, thereby facilitating the electrolyte's diffusion inside the porous network of the graphene film. Second, the well-developed porosity, relatively ordered channels, and 3D conductive network of NG films can substantially improve the use of Ni species. Third, because of the low electron negativity of N atoms, N metal coupling interactions might also be formed to provide additional active centers for catalysis. Finally, the 3D electrode may afford high electrode durability because Ni nanoparticles can be fully accommodated between NG sheets in the film, and their volume change during catalysis can be effectively buffered by adjacent graphene sheets (known for excellent mechanical properties). Because of all these excellent

DOI: 10.1021/acscatal.5b00991
ACS Catal. 2015, 5, 5207−5234

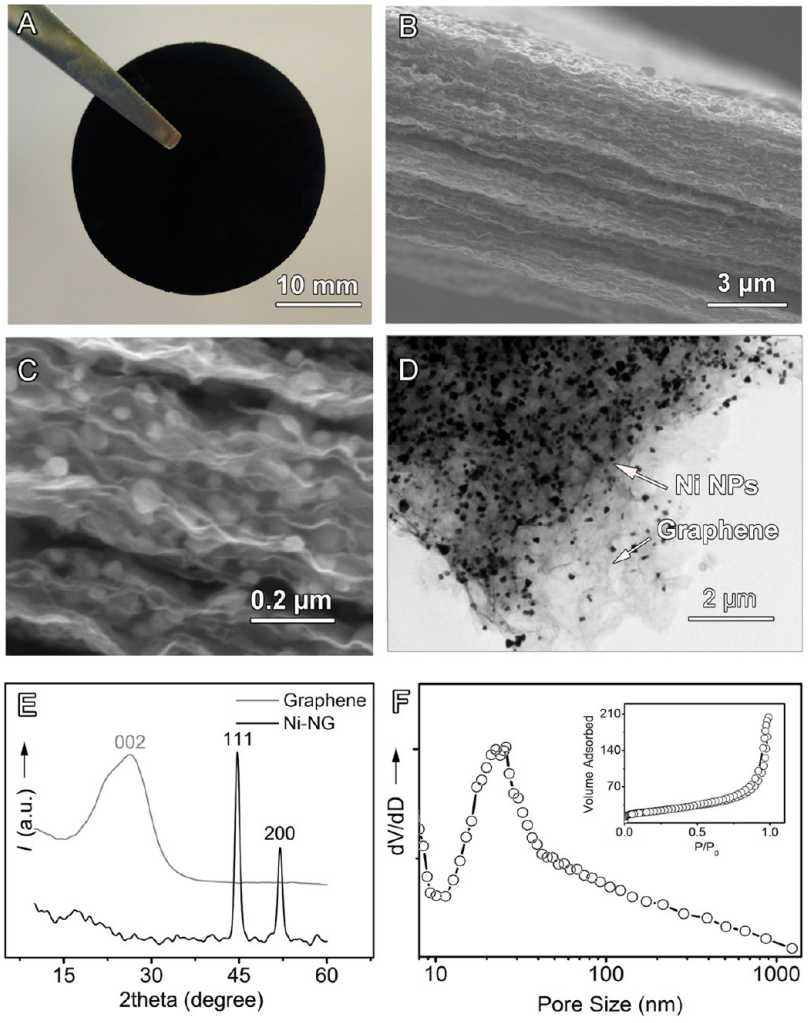

Figure 16. An optical image (a), SEM images of a cross section (b, c), and a TEM image (d); (e) XRD profiles; (f) the pore size distribution (each unit represents 0.005 cm^3 g^{-1} nm^{-1}). The inset in part f shows the corresponding nitrogen adsorption−desorption isotherm (expressed in cm^3 STP g^{-1}) for the hybrid film of NG confined nickel nanoparticles. Reproduced with permission from Qiao et al.[260] Copyright 2013, The Royal Society of Chemistry.

structural properties, the NG−Ni hybrid film electrode affords a surprisingly high catalytic activity toward OER, almost reaching that of the state-of-the-art precious OER electrocatalysts (IrO_2).

Beyond transition metal species, heteroatom-doped graphene has also been hybridized with other nonmetal species, such as nitrogen-doped CNTs[72,264] and graphitic carbons.[265] N-doped CNTs have recently gained a noticeable popularity as low-cost, metal-free catalysts with abundant catalytic sites, environmental compatibility, and strong durability. The strong interactions between graphene and CNTs could inhibit the active species leaching from electrodes and result in strong catalytic durability for OER.[72,264] On the other hand, we recently fabricated a 3D N-doped hybrid carbon film by assembling NG and g-C_3N_4 ultrathin nanosheets on the frameworks of cellulose-based fiber papers.[265] NG shows the high electrical conductivity desirable for fast charge transport, and graphitic carbon ultrathin nanosheets can provide largely exposed active centers for electrocatalysis. Because of the strong synergistic effects between these components and cellulose-based fiber paper, the resulting material can exhibit remarkable catalytic performance, competitive activity and much better durability as compared with the benchmark noble metal electrocatalysts for OER (IrO_2).

Importantly, the corrosion of graphene at high voltage is a concern for its use in OER. Carbon thermodynamically corrodes above 1.8 V; therefore, graphene-based electrocatalysts are usually studied at moderate potentials. Fortunately, these graphene-based electrocatalysts feature strong mechanical stability and can deliver the current density of 10 mA cm^{-2} at a potential of ∼1.6 V. Such a high activity of electrocatalysts is sufficient for integrating them into various renewable energy devices, including photoelectrochemical water splitting cells and solar cells.

6. SUMMARY AND PERSPECTIVES

In summary, a series of doped graphene materials have been reviewed as efficient electrocatalysts for ORR, HER, and OER. The high surface area, excellent mechanical properties, and high conductivity of graphene make it a promising material for electrodes. The heteroatom-doping of graphene with N, B, S, and P can be effectively used to modify its electronic properties and create catalytic active sites by inducing charge and spin densities on C atoms near dopants, consequently affecting the adsorption and desorption abilities of reactants, intermediates

DOI: 10.1021/acscatal.5b00991
ACS Catal. 2015, 5, 5207−5234

and products on the surface of doped graphene, promoting key electrocatalytic reactions such as ORR, HER, and OER. The doped atoms are usually covalently bonded with C atoms of graphene, making doping a robust process that guarantees unparalleled durability in electrocatalysis, rivaling that of noble metals and transition metal-based catalysts. Particularly, the heteroatom-doped graphene materials, used as ORR catalysts in FCs, are resistant to CO poisoning and the methanol crossover effect, which clearly sets them apart from the noble Pt/C electrocatalysts.

In the hybrids consisting of heteroatom-doped graphene and metal compounds, the doped graphene not only acts as the conductive support for anchoring nanoparticles but also, more importantly, contributes to the catalytic activity by providing additional active sites. Significantly, the strong coupling effects are usually present in such hybrids, which not only improve the working stability of electrocatalysts but also enhance their electrocatalytic activity by forming active metal-dopant sites to facilitate electron transfer between the metal and doped graphene. As a result, these hybrid catalysts show comparable—even better—activity and durability as those observed for noble metals.

In addition, 3D heteroatom-doped graphene structures have been reviewed, and some of them can be directly utilized as catalyst electrodes without extra binders and supports. Their remarkable structural properties, such as high specific surface areas, 3D conductive networks, and hierarchical porous structures, can facilitate the electron transport and ion diffusion during electrocatalytic processes, greatly improving the reaction activities and kinetics. Moreover, the 3D free-standing architectures can be used as working electrodes without membrane electrode assembly process, thus avoiding the catalyst agglomeration and peeling off from supports and assuring good activity retention during catalytic processes.

Although significant progress has been made in the field of heteroatom-doped graphene materials for electrocatalytic reactions, there are still some urgent challenges in their large-scale production, controllability of doping configurations, electrocatalytic activity and mechanisms. Specifically, most of the current preparation methods require high temperatures and harsh conditions, which impede large-scale production and commercialization. It is highly desirable to develop a facile and green synthesis of heteroatom-doped graphene based materials. In addition, different doping configurations are known to play diverse roles in electrocatalysis. Nevertheless, there are always several doping structures coexisting in the doped graphene. The controlled synthesis of doped graphene with a single doping configuration is highly desirable to study the effect of one specific configuration on electroactivity. Moreover, despite the currently achieved catalytic activity's being close to that of noble metals such as Pt/C and IrO_2, there is still a big challenge to make the doped graphene materials commercially competitive with noble metals, especially in terms of low-cost synthesis and operation under harsh electrochemical conditions. Furthermore, the reaction mechanisms are still inconclusive in many electrochemical systems because of the continuous development of new materials and advanced applications. We believe that further explorations in this exciting area of doped graphene materials will contribute to green energy systems, and all the above problems will be solved.

AUTHOR INFORMATION

Corresponding Author

*E-mail: s.qiao@adelaide.edu.au.

Notes

The authors declare no competing financial interest.

ACKNOWLEDGMENTS

This work was financially supported by the Australian Research Council (ARC) through the Discovery Project program (DP 130104459, DP 140104062).

REFERENCES

(1) Frumkin, A.; Polianov, N.; Bagotska, I.; Grigorye, N. *J. Electroanal. Chem. Interfacial Electrochem.* **1971**, *33*, 319−328.
(2) Azzam, A. M.; Bockris, J. O. *Nature* **1950**, *165*, 403−404.
(3) Juttner, K. *Electrochim. Acta* **1986**, *31*, 917−927.
(4) Novoselov, K. S.; Geim, A. K.; Morozov, S. V.; Jiang, D.; Zhang, Y.; Dubonos, S. V.; Grigorieva, I. V.; Firsov, A. A. *Science* **2004**, *306*, 666−669.
(5) Geim, A. K.; Novoselov, K. S. *Nat. Mater.* **2007**, *6*, 183−191.
(6) Obraztsov, A. N. *Nat. Nanotechnol.* **2009**, *4*, 212−213.
(7) Hernandez, Y.; Nicolosi, V.; Lotya, M.; Blighe, F. M.; Sun, Z.; De, S.; McGovern, I. T.; Holland, B.; Byrne, M.; Gun'Ko, Y. K.; Boland, J. J.; Niraj, P.; Duesberg, G.; Krishnamurthy, S.; Goodhue, R.; Hutchison, J.; Scardaci, V.; Ferrari, A. C.; Coleman, J. N. *Nat. Nanotechnol.* **2008**, *3*, 563−568.
(8) Hummers, W. S.; Offeman, R. E. *J. Am. Chem. Soc.* **1958**, *80*, 1339−1339.
(9) Li, D.; Müller, M. B.; Gilje, S.; Kaner, R. B.; Wallace, G. G. *Nat. Nanotechnol.* **2008**, *3*, 101.
(10) Sun, Z.; Yan, Z.; Yao, J.; Beitler, E.; Zhu, Y.; Tour, J. M. *Nature* **2010**, *468*, 549−552.
(11) Ruan, G.; Sun, Z.; Peng, Z.; Tour, J. M. *ACS Nano* **2011**, *5*, 7601−7607.
(12) Wu, J.; Pisula, W.; Müllen, K. *Chem. Rev.* **2007**, *107*, 718−747.
(13) Stoller, M. D.; Park, S.; Zhu, Y.; An, J.; Ruoff, R. S. *Nano Lett.* **2008**, *8*, 3498−3502.
(14) Sahoo, N. G.; Pan, Y.; Li, L.; Chan, S. H. *Adv. Mater.* **2012**, *24*, 4203−4210.
(15) Boukhvalov, D. W.; Katsnelson, M. I. *Nano Lett.* **2008**, *8*, 4373−4379.
(16) Guell, A. G.; Ebejer, N.; Snowden, M. E.; Macpherson, J. V.; Unwin, P. R. *J. Am. Chem. Soc.* **2012**, *134*, 7258−7261.
(17) Chang, C.-H.; Fan, X.; Li, L.-J.; Kuo, J.-L. *J. Phys. Chem. C* **2012**, *116*, 13788−13794.
(18) Ritter, K. A.; Lyding, J. W. *Nat. Mater.* **2009**, *8*, 235−242.
(19) Yan, X.; Cui, X.; Li, L. S. *J. Am. Chem. Soc.* **2010**, *132*, 5944−5945.
(20) Glerup, M.; Castignolles, M.; Holzinger, M.; Hug, G.; Loiseau, A.; Bernier, P. *Chem. Commun.* **2003**, 2542−2543.
(21) Cervantes-Sodi, F.; Csányi, G.; Piscanec, S.; Ferrari, A. *Phys. Rev. B: Condens. Matter Mater. Phys.* **2008**, *77*, 165427.
(22) Wang, H.; Maiyalagan, T.; Wang, X. *ACS Catal.* **2012**, *2*, 781−794.
(23) Yang, D. S.; Song, M. Y.; Singh, K. P.; Yu, J. S. *Chem. Commun.* **2015**, *51*, 2450−2453.
(24) Georgakilas, V.; Otyepka, M.; Bourlinos, A. B.; Chandra, V.; Kim, N.; Kemp, K. C.; Hobza, P.; Zboril, R.; Kim, K. S. *Chem. Rev.* **2012**, *112*, 6156−6214.
(25) Dai, L.; Xue, Y.; Qu, L.; Choi, H. J.; Baek, J. B. *Chem. Rev.* **2015**, *115*, 4823−4892.
(26) Li, Q.; Mahmood, N.; Zhu, J.; Hou, Y.; Sun, S. *Nano Today* **2014**, *9*, 668−683.
(27) Wang, X.; Sun, G.; Routh, P.; Kim, D. H.; Huang, W.; Chen, P. *Chem. Soc. Rev.* **2014**, *43*, 7067−7098.
(28) Kong, X. K.; Chen, C. L.; Chen, Q. W. *Chem. Soc. Rev.* **2014**, *43*, 2841−2857.

DOI: 10.1021/acscatal.5b00991
ACS Catal. 2015, 5, 5207−5234

(29) Liu, H.; Liu, Y.; Zhu, D. *J. Mater. Chem.* **2011**, *21*, 3335−3345.
(30) Debe, M. K. *Nature* **2012**, *486*, 43−51.
(31) Chen, Z.; Higgins, D.; Yu, A.; Zhang, L.; Zhang, J. *Energy Environ. Sci.* **2011**, *4*, 3167−3192.
(32) Stamenkovic, V. R.; Fowler, B.; Mun, B. S.; Wang, G.; Ross, P. N.; Lucas, C. A.; Markovic, N. M. *Science* **2007**, *315*, 493−497.
(33) Chou, S.-W.; Shyue, J.-J.; Chien, C.-H.; Chen, C.-C.; Chen, Y.-Y.; Chou, P.-T. *Chem. Mater.* **2012**, *24*, 2527−2533.
(34) Vinayan, B. P.; Nagar, R.; Rajalakshmi, N.; Ramaprabhu, S. *Adv. Funct. Mater.* **2012**, *22*, 3519−3526.
(35) Paulus, U. A.; Schmidt, T. J.; Gasteiger, H. A.; Behm, R. J. *J. Electroanal. Chem.* **2001**, *495*, 134−145.
(36) U.S. Department of Energy. http://energy.gov/sites/prod/files/2014/02/f8/fctt_roadmap_june2013.pdf.
(37) Turner, J. A. *Science* **2004**, *305*, 972−974.
(38) Greeley, J.; Jaramillo, T. F.; Bonde, J.; Chorkendorff, I. B.; Nørskov, J. K. *Nat. Mater.* **2006**, *5*, 909−913.
(39) Lin, S. Y.; Harada, M.; Suzuki, Y.; Hatano, H. *Fuel* **2002**, *81*, 2079−2085.
(40) Oertel, M.; Schmitz, J.; Weirich, W.; Jendryssek-Neumann, D.; Schulten, R. *Chem. Eng. Technol.* **1987**, *10*, 248−255.
(41) Carver, S. M.; Hulatt, C. J.; Thomas, D. N.; Tuovinen, O. H. *Biodegradation* **2011**, *22*, 805−814.
(42) Thomas, J. G. N. *Trans. Faraday Soc.* **1961**, *57*, 1603−1611.
(43) Sheng, W.; Zhuang, Z.; Gao, M.; Zheng, J.; Chen, J. G.; Yan, Y. *Nat. Commun.* **2015**, *6*, 5848−5853.
(44) McKone, J. R.; Sadtler, B. F.; Werlang, C. A.; Lewis, N. S.; Gray, H. B. *ACS Catal.* **2013**, *3*, 166−169.
(45) Jaramillo, T. F.; Jorgensen, K. P.; Bonde, J.; Nielsen, J. H.; Horch, S.; Chorkendorff, I. *Science* **2007**, *317*, 100−102.
(46) Huang, Z.; Chen, Z.; Chen, Z.; Lv, C.; Meng, H.; Zhang, C. *ACS Nano* **2014**, *8*, 8121−8129.
(47) Vrubel, H.; Hu, X. *Angew. Chem., Int. Ed.* **2012**, *51*, 12703−12706.
(48) Chen, W. F.; Sasaki, K.; Ma, C.; Frenkel, A. I.; Marinkovic, N.; Muckerman, J. T.; Zhu, Y.; Adzic, R. R. *Angew. Chem., Int. Ed.* **2012**, *51*, 6131−6135.
(49) Tian, J.; Liu, Q.; Asiri, A. M.; Sun, X. *J. Am. Chem. Soc.* **2014**, *136*, 7587−7590.
(50) Duan, J.; Chen, S.; Jaroniec, M.; Qiao, S. Z. *ACS Nano* **2015**, *9*, 931−940.
(51) Armand, M.; Tarascon, J. M. *Nature* **2008**, *451*, 652−657.
(52) Gray, H. B. *Nat. Chem.* **2009**, *1*, 7.
(53) Li, Y.; Dai, H. *Chem. Soc. Rev.* **2014**, *43*, 5257−5275.
(54) Qiao, J.; Liu, Y.; Hong, F.; Zhang, J. *Chem. Soc. Rev.* **2014**, *43*, 631−675.
(55) Liang, Y.; Li, Y.; Wang, H.; Zhou, J.; Wang, J.; Regier, T.; Dai, H. *Nat. Mater.* **2011**, *10*, 780−786.
(56) Mirzakulova, E.; Khatmullin, R.; Walpita, J.; Corrigan, T.; Vargas-Barbosa, N. M.; Vyas, S.; Oottikkal, S.; Manzer, S. F.; Hadad, C. M.; Glusac, K. D. *Nat. Chem.* **2012**, *4*, 794−801.
(57) Suntivich, J.; May, K. J.; Gasteiger, H. A.; Goodenough, J. B.; Shao-Horn, Y. *Science* **2011**, *334*, 1383−1385.
(58) Yin, Q.; Tan, J. M.; Besson, C.; Geletii, Y. V.; Musaev, D. G.; Kuznetsov, A. E.; Luo, Z.; Hardcastle, K. I.; Hill, C. L. *Science* **2010**, *328*, 342−345.
(59) Abdelhafiz, A.; Vitale, A.; Joiner, C.; Vogel, E.; Alamgir, F. M. *ACS Appl. Mater. Interfaces* **2015**, *7*, 6180−6188.
(60) Ardizzone, S.; Fregonara, G.; Trasatti, S. *Electrochim. Acta* **1990**, *35*, 263−267.
(61) Cherevko, S.; Zeradjanin, A. R.; Topalov, A. A.; Kulyk, N.; Katsounaros, I.; Mayrhofer, K. J. J. *ChemCatChem* **2014**, *6*, 2219−2223.
(62) Jiao, Y.; Zheng, Y.; Jaroniec, M.; Qiao, S. Z. *Chem. Soc. Rev.* **2015**, *44*, 2060−2086.
(63) Hong, J.; Kang, S. W.; Choi, B.-S.; Kim, D.; Lee, S. B.; Han, S. W. *ACS Nano* **2012**, *6*, 2410−2419.
(64) Nong, H. N.; Oh, H. S.; Reier, T.; Willinger, E.; Willinger, M. G.; Petkov, V.; Teschner, D.; Strasser, P. *Angew. Chem., Int. Ed.* **2015**, *54*, 2975−2979.
(65) Sardar, K.; Petrucco, E.; Hiley, C. I.; Sharman, J. D.; Wells, P. P.; Russell, A. E.; Kashtiban, R. J.; Sloan, J.; Walton, R. I. *Angew. Chem., Int. Ed.* **2014**, *53*, 10960−10964.
(66) Bergmann, A.; Zaharieva, I.; Dau, H.; Strasser, P. *Energy Environ. Sci.* **2013**, *6*, 2745−2755.
(67) Gong, M.; Li, Y.; Wang, H.; Liang, Y.; Wu, J. Z.; Zhou, J.; Wang, J.; Regier, T.; Wei, F.; Dai, H. *J. Am. Chem. Soc.* **2013**, *135*, 8452−8455.
(68) Kanan, M. W.; Nocera, D. G. *Science* **2008**, *321*, 1072−1075.
(69) Zhao, Y.; Nakamura, R.; Kamiya, K.; Nakanishi, S.; Hashimoto, K. *Nat. Commun.* **2013**, *4*, 2390−2396.
(70) Chen, S.; Qiao, S. Z. *ACS Nano* **2013**, *7*, 10190−10196.
(71) Jin, H.; Wang, J.; Su, D.; Wei, Z.; Pang, Z.; Wang, Y. *J. Am. Chem. Soc.* **2015**, *137*, 2688−2694.
(72) Tian, G. L.; Zhao, M. Q.; Yu, D.; Kong, X. Y.; Huang, J. Q.; Zhang, Q.; Wei, F. *Small* **2014**, *10*, 2251−2259.
(73) Barnett, S. M.; Goldberg, K. I.; Mayer, J. M. *Nat. Chem.* **2012**, *4*, 498−502.
(74) Fillol, J. L.; Codolà, Z.; Garcia-Bosch, I.; Gómez, L.; Pla, J. J.; Costas, M. *Nat. Chem.* **2011**, *3*, 807−813.
(75) Geletii, Y. V.; Botar, B.; Kogerler, P.; Hillesheim, D. A.; Musaev, D. G.; Hill, C. L. *Angew. Chem., Int. Ed.* **2008**, *47*, 3896−3899.
(76) Jiang, Y.; Li, F.; Zhang, B.; Li, X.; Wang, X.; Huang, F.; Sun, L. *Angew. Chem., Int. Ed.* **2013**, *52*, 3398−3401.
(77) Singh, A.; Chang, S. L. Y.; Hocking, R. K.; Bach, U.; Spiccia, L. *Energy Environ. Sci.* **2013**, *6*, 579−586.
(78) Toma, F. M.; Sartorel, A.; Iurlo, M.; Carraro, M.; Parisse, P.; Maccato, C.; Rapino, S.; Gonzalez, B. R.; Amenitsch, H.; Da Ros, T.; Casalis, L.; Goldoni, A.; Marcaccio, M.; Scorrano, G.; Scoles, G.; Paolucci, F.; Prato, M.; Bonchio, M. *Nat. Chem.* **2010**, *2*, 826−831.
(79) Li, Y.; Zhou, Z.; Shen, P.; Chen, Z. *ACS Nano* **2009**, *3*, 1952−1958.
(80) Biddinger, E. J.; von Deak, D.; Ozkan, U. S. *Top. Catal.* **2009**, *52*, 1566−1574.
(81) Sheng, Z. H.; Shao, L.; Chen, J. J.; Bao, W. J.; Wang, F. B.; Xia, X. H. *ACS Nano* **2011**, *5*, 4350−4358.
(82) Deng, D.; Pan, X.; Yu, L.; Cui, Y.; Jiang, Y.; Qi, J.; Li, W.-X.; Fu, Q.; Ma, X.; Xue, Q.; Sun, G.; Bao, X. *Chem. Mater.* **2011**, *23*, 1188−1193.
(83) Artyushkova, K.; Atanassov, P. *ChemPhysChem* **2013**, *14*, 2071−2080.
(84) Sun, L.; Wang, L.; Tian, C.; Tan, T.; Xie, Y.; Shi, K.; Li, M.; Fu, H. *RSC Adv.* **2012**, *2*, 4498−4506.
(85) Jin, Z.; Yao, J.; Kittrell, C.; Tour, J. M. *ACS Nano* **2011**, *5*, 4112−4117.
(86) Wang, X.; Li, X.; Zhang, L.; Yoon, Y.; Weber, P. K.; Wang, H.; Guo, J.; Dai, H. *Science* **2009**, *324*, 768−771.
(87) Li, X.; Wang, H.; Robinson, J. T.; Sanchez, H.; Diankov, G.; Dai, H. *J. Am. Chem. Soc.* **2009**, *131*, 15939−15944.
(88) Panchakarla, L. S.; Subrahmanyam, K. S.; Saha, S. K.; Govindaraj, A.; Krishnamurthy, H. R.; Waghmare, U. V.; Rao, C. N. R. *Adv. Mater.* **2009**, *21*, 4726−4730.
(89) Zhang, C.; Fu, L.; Liu, N.; Liu, M.; Wang, Y.; Liu, Z. *Adv. Mater.* **2011**, *23*, 1020−1024.
(90) Shao, Y.; Zhang, S.; Engelhard, M. H.; Li, G.; Shao, G.; Wang, Y.; Liu, J.; Aksay, I. A.; Lin, Y. *J. Mater. Chem.* **2010**, *20*, 7491−7496.
(91) Zhao, Y.; Hu, C.; Hu, Y.; Cheng, H.; Shi, G.; Qu, L. *Angew. Chem., Int. Ed.* **2012**, *51*, 11371−11375.
(92) Pan, F.; Jin, J.; Fu, X.; Liu, Q.; Zhang, J. *ACS Appl. Mater. Interfaces* **2013**, *5*, 11108−11114.
(93) Luo, Z.; Lim, S.; Tian, Z.; Shang, J.; Lai, L.; MacDonald, B.; Fu, C.; Shen, Z.; Yu, T.; Lin, J. *J. Mater. Chem.* **2011**, *21*, 8038−8044.
(94) Wei, D.; Liu, Y.; Wang, Y.; Zhang, H.; Huang, L.; Yu, G. *Nano Lett.* **2009**, *9*, 1752−1758.
(95) Zhao, L.; He, R.; Rim, K. T.; Schiros, T.; Kim, K. S.; Zhou, H.; Gutierrez, C.; Chockalingam, S. P.; Arguello, C. J.; Palova, L.;

DOI: 10.1021/acscatal.5b00991
ACS Catal. 2015, 5, 5207−5234

Nordlund, D.; Hybertsen, M. S.; Reichman, D. R.; Heinz, T. F.; Kim, P.; Pinczuk, A.; Flynn, G. W.; Pasupathy, A. N. *Science* **2011**, *333*, 999−1003.
(96) Usachov, D.; Vilkov, O.; Gruneis, A.; Haberer, D.; Fedorov, A.; Adamchuk, V. K.; Preobrajenski, A. B.; Dudin, P.; Barinov, A.; Oehzelt, M.; Laubschat, C.; Vyalikh, D. V. *Nano Lett.* **2011**, *11*, 5401−5407.
(97) Qu, L.; Liu, Y.; Baek, J.-B.; Dai, L. *ACS Nano* **2010**, *4*, 1321−1326.
(98) Xue, Y.; Wu, B.; Jiang, L.; Guo, Y.; Huang, L.; Chen, J.; Tan, J.; Geng, D.; Luo, B.; Hu, W.; Yu, G.; Liu, Y. *J. Am. Chem. Soc.* **2012**, *134*, 11060−11063.
(99) Long, D.; Li, W.; Ling, L.; Miyawaki, J.; Mochida, I.; Yoon, S. H. *Langmuir* **2010**, *26*, 16096−16102.
(100) Qian, W.; Cui, X.; Hao, R.; Hou, Y.; Zhang, Z. *ACS Appl. Mater. Interfaces* **2011**, *3*, 2259−2264.
(101) Zhao, W.; Höfert, O.; Gotterbarm, K.; Zhu, J. F.; Papp, C.; Steinrück, H. P. *J. Phys. Chem. C* **2012**, *116*, 5062−5066.
(102) Jeon, I. Y.; Choi, H. J.; Ju, M. J.; Choi, I. T.; Lim, K.; Ko, J.; Kim, H. K.; Kim, J. C.; Lee, J. J.; Shin, D.; Jung, S. M.; Seo, J. M.; Kim, M. J.; Park, N.; Dai, L.; Baek, J. B. *Sci. Rep.* **2013**, *3*, 2260.
(103) Tang, Y. B.; Yin, L. C.; Yang, Y.; Bo, X. H.; Cao, Y. L.; Wang, H. E.; Zhang, W. J.; Bello, I.; Lee, S. T.; Cheng, H. M.; Lee, C. S. *ACS Nano* **2012**, *6*, 1970−1978.
(104) Faccio, R.; Fernandez-Werner, L.; Pardo, H.; Goyenola, C.; Ventura, O. N.; Mombru, A. W. *J. Phys. Chem. C* **2010**, *114*, 18961−18971.
(105) Li, X.; Fan, L.; Li, Z.; Wang, K.; Zhong, M.; Wei, J.; Wu, D.; Zhu, H. *Adv. Enerry Mater.* **2012**, *2*, 425−429.
(106) Yu, S.; Zheng, W.; Wang, C.; Jiang, Q. *ACS Nano* **2010**, *4*, 7619−7629.
(107) Lü, X.; Wu, J.; Lin, T.; Wan, D.; Huang, F.; Xie, X.; Jiang, M. *J. Mater. Chem.* **2011**, *21*, 10685−10689.
(108) Zhao, L.; Levendorf, M.; Goncher, S.; Schiros, T.; Palova, L.; Zabet-Khosousi, A.; Rim, K. T.; Gutierrez, C.; Nordlund, D.; Jaye, C.; Hybertsen, M.; Reichman, D.; Flynn, G. W.; Park, J.; Pasupathy, A. N. *Nano Lett.* **2013**, *13*, 4659−4665.
(109) Kim, Y. A.; Fujisawa, K.; Muramatsu, H.; Hayashi, T.; Endo, M.; Fujimori, T.; Kaneko, K.; Terrones, M.; Behrends, J.; Eckmann, A.; Casiraghi, C.; Novoselov, K. S.; Saito, R.; Dresselhaus, M. S. *ACS Nano* **2012**, *6*, 6293−6300.
(110) Dou, C.; Saito, S.; Matsuo, K.; Hisaki, I.; Yamaguchi, S. *Angew. Chem., Int. Ed.* **2012**, *51*, 12206−12210.
(111) Cattelan, M.; Agnoli, S.; Favaro, M.; Garoli, D.; Romanato, F.; Meneghetti, M.; Barinov, A.; Dudin, P.; Granozzi, G. *Chem. Mater.* **2013**, *25*, 1490−1495.
(112) Wang, H.; Zhou, Y.; Wu, D.; Liao, L.; Zhao, S.; Peng, H.; Liu, Z. *Small* **2013**, *9*, 1316−1320.
(113) Yen, W.-C.; Medina, H.; Huang, J.-S.; Lai, C.-C.; Shih, Y.-C.; Lin, S.-M.; Li, J.-G.; Wang, Z. M.; Chueh, Y.-L. *J. Phys. Chem. C* **2014**, *118*, 25089−25096.
(114) Han, J.; Zhang, L. L.; Lee, S.; Oh, J.; Lee, K. S.; Potts, J. R.; Ji, J. Y.; Zhao, X.; Ruoff, R. S.; Park, S. *ACS Nano* **2013**, *7*, 19−26.
(115) Denis, P. A.; Faccio, R.; Mombru, A. W. *ChemPhysChem* **2009**, *10*, 715−722.
(116) Zhang, L.; Niu, J.; Li, M.; Xia, Z. *J. Phys. Chem. C* **2014**, *118*, 3545−3553.
(117) Jeon, I. Y.; Zhang, S.; Zhang, L.; Choi, H. J.; Seo, J. M.; Xia, Z.; Dai, L.; Baek, J. B. *Adv. Mater.* **2013**, *25*, 6138−6145.
(118) Poh, H. L.; Simek, P.; Sofer, Z.; Pumera, M. *ACS Nano* **2013**, *7*, 5262−5272.
(119) Wang, Z.; Li, P.; Chen, Y.; He, J.; Zhang, W.; Schmidt, O. G.; Li, Y. *Nanoscale* **2014**, *6*, 7281−7287.
(120) Yang, Z.; Yao, Z.; Li, G. F.; Fang, G. Y.; Nie, H. G.; Liu, Z.; Zhou, X. M.; Chen, X.; Huang, S. M. *ACS Nano* **2012**, *6*, 205−211.
(121) Li, M.; Liu, C.; Zhao, H.; An, H.; Cao, H.; Zhang, Y.; Fan, Z. *Carbon* **2015**, *86*, 197−206.
(122) Wang, R.; Higgins, D. C.; Hoque, M. A.; Lee, D.; Hassan, F.; Chen, Z. *Sci. Rep.* **2013**, *3*, 2431−2437.
(123) Li, X.; Lau, S. P.; Tang, L.; Ji, R.; Yang, P. *Nanoscale* **2014**, *6*, 5323−5328.
(124) Liu, Y.; Ma, Y.; Jin, Y.; Chen, G.; Zhang, X. *J. Electroanal. Chem.* **2015**, *739*, 172−177.
(125) Ma, Z.; Dou, S.; Shen, A.; Tao, L.; Dai, L.; Wang, S. *Angew. Chem., Int. Ed.* **2015**, *54*, 1888−1892.
(126) Zhang, Y.; Chu, M.; Yang, L.; Deng, W.; Tan, Y.; Ma, M.; Xie, Q. *Chem. Commun.* **2014**, *50*, 6382−6385.
(127) Li, S.; Li, Y.; Cao, J.; Zhu, J.; Fan, L.; Li, X. *Anal. Chem.* **2014**, *86*, 10201−10207.
(128) Yang, D.-S.; Bhattacharjya, D.; Song, M. Y.; Yu, J.-S. *Carbon* **2014**, *67*, 736−743.
(129) Cruz-Silva, E.; Lopez-Urias, F.; Munoz-Sandoval, E.; Sumpter, B. G.; Terrones, H.; Charlier, J. C.; Meunier, V.; Terrones, M. *ACS Nano* **2009**, *3*, 1913−1921.
(130) Wang, H. M.; Wang, H. X.; Chen, Y.; Liu, Y. J.; Zhao, J. X.; Cai, Q. H.; Wang, X. Z. *Appl. Surf. Sci.* **2013**, *273*, 302−309.
(131) Dai, J.; Yuan, J. *J. Phys.: Condens. Matter* **2010**, *22*, 225501−225506.
(132) Wu, J.; Yang, Z.; Sun, Q.; Li, X.; Strasser, P.; Yang, R. *Electrochim. Acta* **2014**, *127*, 53−60.
(133) Latorre-Sanchez, M.; Primo, A.; Garcia, H. *Angew. Chem., Int. Ed.* **2013**, *52*, 11813−11816.
(134) Some, S.; Kim, J.; Lee, K.; Kulkarni, A.; Yoon, Y.; Lee, S.; Kim, T.; Lee, H. *Adv. Mater.* **2012**, *24*, 5481−5486.
(135) Li, R.; Wei, Z.; Gou, X.; Xu, W. *RSC Adv.* **2013**, *3*, 9978−9984.
(136) Zhang, C.; Mahmood, N.; Yin, H.; Liu, F.; Hou, Y. *Adv. Mater.* **2013**, *25*, 4932−4937.
(137) Wen, Y.; Wang, B.; Huang, C.; Wang, L.; Hulicova-Jurcakova, D. *Chem. - Eur. J.* **2015**, *21*, 80−85.
(138) Poh, H. L.; Sofer, Z.; Novacek, M.; Pumera, M. *Chem. - Eur. J.* **2014**, *20*, 4284−4291.
(139) Sen, D.; Thapa, R.; Chattopadhyay, K. K. *ChemPhysChem* **2014**, *15*, 2542−2549.
(140) Li, X. H.; Antonietti, M. *Angew. Chem., Int. Ed.* **2013**, *52*, 4572−4576.
(141) Lin, T. W.; Su, C. Y.; Zhang, X. Q.; Zhang, W.; Lee, Y. H.; Chu, C. W.; Lin, H. Y.; Chang, M. T.; Chen, F. R.; Li, L. J. *Small* **2012**, *8*, 1384−1391.
(142) Byeon, A.; Lee, J. W. *J. Phys. Chem. C* **2013**, *117*, 24167−24173.
(143) Zheng, Y.; Jiao, Y.; Ge, L.; Jaroniec, M.; Qiao, S. Z. *Angew. Chem., Int. Ed.* **2013**, *52*, 3110−3116.
(144) Wang, S.; Zhang, L.; Xia, Z.; Roy, A.; Chang, D. W.; Baek, J. B.; Dai, L. *Angew. Chem., Int. Ed.* **2012**, *51*, 4209−4212.
(145) Favaro, M.; Ferrighi, L.; Fazio, G.; Colazzo, L.; Di Valentin, C.; Durante, C.; Sedona, F.; Gennaro, A.; Agnoli, S.; Granozzi, G. *ACS Catal.* **2015**, *5*, 129−144.
(146) Jin, J.; Pan, F.; Jiang, L.; Fu, X.; Liang, A.; Wei, Z.; Zhang, J.; Sun, G. *ACS Nano* **2014**, *8*, 3313−3321.
(147) Wang, S.; Iyyamperumal, E.; Roy, A.; Xue, Y.; Yu, D.; Dai, L. *Angew. Chem., Int. Ed.* **2011**, *50*, 11756−11760.
(148) Wu, Z. S.; Winter, A.; Chen, L.; Sun, Y.; Turchanin, A.; Feng, X.; Müllen, K. *Adv. Mater.* **2012**, *24*, 5130−5135.
(149) Xu, J.; Dong, G.; Jin, C.; Huang, M.; Guan, L. *ChemSusChem* **2013**, *6*, 493−499.
(150) Ito, Y.; Cong, W.; Fujita, T.; Tang, Z.; Chen, M. *Angew. Chem., Int. Ed.* **2015**, *54*, 2131−2136.
(151) Liang, J.; Jiao, Y.; Jaroniec, M.; Qiao, S. Z. *Angew. Chem., Int. Ed.* **2012**, *51*, 11496−11500.
(152) Ai, W.; Luo, Z.; Jiang, J.; Zhu, J.; Du, Z.; Fan, Z.; Xie, L.; Zhang, H.; Huang, W.; Yu, T. *Adv. Mater.* **2014**, *26*, 6186−6192.
(153) Xiao, P.; Yan, Y.; Ge, X.; Liu, Z.; Wang, J.-Y.; Wang, X. *Appl. Catal., B* **2014**, *154*−*155*, 232−237.
(154) Zhang, H.; Liu, X.; He, G.; Zhang, X.; Bao, S.; Hu, W. *J. Power Sources* **2015**, *279*, 252−258.
(155) Kannan, A. G.; Zhao, J.; Jo, S. G.; Kang, Y. S.; Kim, D.-W. *J. Mater. Chem. A* **2014**, *2*, 12232−12239.

DOI: 10.1021/acscatal.5b00991
ACS Catal. 2015, 5, 5207−5234

(156) Li, Y.; Li, M.; Jiang, L.; Lin, L.; Cui, L.; He, X. *Phys. Chem. Chem. Phys.* **2014**, *16*, 23196−23205.
(157) Wang, X.; Wang, J.; Wang, D.; Dou, S.; Ma, Z.; Wu, J.; Tao, L.; Shen, A.; Ouyang, C.; Liu, Q.; Wang, S. *Chem. Commun.* **2014**, *50*, 4839−4842.
(158) Feng, B.; Xie, J.; Dong, C.; Zhang, S.; Cao, G.; Zhao, X. *RSC Adv.* **2014**, *4*, 17902−17907.
(159) Luo, Q.; Hao, F.; Wang, S.; Shen, H.; Zhao, L.; Li, J.; Grätzel, M.; Lin, H. *J. Phys. Chem. C* **2014**, *118*, 17010−17018.
(160) Ma, X.; Ning, G.; Qi, C.; Xu, C.; Gao, J. *ACS Appl. Mater. Interfaces* **2014**, *6*, 14415−14422.
(161) Xue, Y.; Wu, B.; Liu, H.; Tan, J.; Hu, W.; Liu, Y. *Phys. Chem. Chem. Phys.* **2014**, *16*, 20392−20397.
(162) Razmjooei, F.; Singh, K. P.; Song, M. Y.; Yu, J.-S. *Carbon* **2014**, *78*, 257−267.
(163) Yao, Z.; Nie, H.; Yang, Z.; Zhou, X.; Liu, Z.; Huang, S. *Chem. Commun.* **2012**, *48*, 1027−1029.
(164) Matis, B. R.; Burgess, J. S.; Bulat, F. A.; Friedman, A. L.; Houston, B. H.; Baldwin, J. W. *ACS Nano* **2012**, *6*, 17−22.
(165) Paulus, U. A.; Schmidt, T. J.; Gasteiger, H. A.; Behm, R. J. *J. Electroanal. Chem.* **2001**, *495*, 134−145.
(166) Dathar, G. K. P.; Shelton, W. A.; Xu, Y. *J. Phys. Chem. Lett.* **2012**, *3*, 891−895.
(167) Zhang, J.; Sasaki, K.; Sutter, E.; Adzic, R. R. *Science* **2007**, *315*, 220−222.
(168) Service, R. F. *Science* **2007**, *315*, 172.
(169) Deng, D.; Yu, L.; Chen, X.; Wang, G.; Jin, L.; Pan, X.; Deng, J.; Sun, G.; Bao, X. *Angew. Chem., Int. Ed.* **2013**, *52*, 371−375.
(170) Bashyam, R.; Zelenay, P. *Nature* **2006**, *443*, 63−66.
(171) Liang, J.; Zhou, R. F.; Chen, X. M.; Tang, Y. H.; Qiao, S. Z. *Adv. Mater.* **2014**, *26*, 6074−6079.
(172) Lee, J. S.; Park, G. S.; Lee, H. I.; Kim, S. T.; Cao, R.; Liu, M.; Cho, J. *Nano Lett.* **2011**, *11*, 5362−5366.
(173) Wang, H.; Liang, Y.; Li, Y.; Dai, H. *Angew. Chem., Int. Ed.* **2011**, *50*, 10969−10972.
(174) Hu, Y.; Jensen, J. O.; Zhang, W.; Cleemann, L. N.; Xing, W.; Bjerrum, N. J.; Li, Q. *Angew. Chem., Int. Ed.* **2014**, *53*, 3675−3679.
(175) Gong, K.; Du, F.; Xia, Z.; Durstock, M.; Dai, L. *Science* **2009**, *323*, 760−764.
(176) Zheng, Y.; Jiao, Y.; Chen, J.; Liu, J.; Liang, J.; Du, A.; Zhang, W.; Zhu, Z.; Smith, S. C.; Jaroniec, M.; Lu, G. Q.; Qiao, S. Z. *J. Am. Chem. Soc.* **2011**, *133*, 20116−20119.
(177) Liang, Y.; Wang, H.; Zhou, J.; Li, Y.; Wang, J.; Regier, T.; Dai, H. *J. Am. Chem. Soc.* **2012**, *134*, 3517−3523.
(178) Jiao, Y.; Zheng, Y.; Jaroniec, M.; Qiao, S. Z. *J. Am. Chem. Soc.* **2014**, *136*, 4394−4403.
(179) Saidi, W. A. *J. Phys. Chem. Lett.* **2013**, *4*, 4160−4165.
(180) Bo, X.; Han, C.; Zhang, Y.; Guo, L. *ACS Appl. Mater. Interfaces* **2014**, *6*, 3023−3030.
(181) Zhou, R.; Qiao, S. Z. *Chem. Mater.* **2014**, *26*, 5868−5873.
(182) Kim, G.; Jhi, S.-H.; Park, N. *Appl. Phys. Lett.* **2008**, *92*, 013106.
(183) Parvez, K.; Yang, S.; Hernandez, Y.; Winter, A.; Turchanin, A.; Feng, X.; Müllen, K. *ACS Nano* **2012**, *6*, 9541−9550.
(184) Duan, J.; Zheng, Y.; Chen, S.; Tang, Y.; Jaroniec, M.; Qiao, S. *Chem. Commun.* **2013**, *49*, 7705−7707.
(185) Duan, J.; Chen, S.; Dai, S.; Qiao, S. Z. *Adv. Funct. Mater.* **2014**, *24*, 2072−2078.
(186) Zhou, R.; Zheng, Y.; Hulicova-Jurcakova, D.; Qiao, S. Z. *J. Mater. Chem. A* **2013**, *1*, 13179−13185.
(187) Wu, Z. S.; Yang, S.; Sun, Y.; Parvez, K.; Feng, X.; Müllen, K. *J. Am. Chem. Soc.* **2012**, *134*, 9082−9085.
(188) Chen, P.; Xiao, T. Y.; Li, H. H.; Yang, J. J.; Wang, Z.; Yao, H. B.; Yu, S. H. *ACS Nano* **2012**, *6*, 712−719.
(189) Yin, H.; Zhang, C.; Liu, F.; Hou, Y. *Adv. Funct. Mater.* **2014**, *24*, 2930−2937.
(190) Kong, X.; Chen, Q.; Sun, Z. *ChemPhysChem* **2013**, *14*, 514−519.
(191) del Cueto, M.; Ocón, P.; Poyato, J. M. L. *J. Phys. Chem. C* **2015**, *119*, 2004−2009.
(192) Ferrighi, L.; Datteo, M.; Di Valentin, C. *J. Phys. Chem. C* **2014**, *118*, 223−230.
(193) Wang, L.; Sofer, Z.; Šimek, P.; Tomandl, I.; Pumera, M. *J. Phys. Chem. C* **2013**, *117*, 23251−23257.
(194) Park, J. E.; Jang, Y. J.; Kim, Y. J.; Song, M. S.; Yoon, S.; Kim, D. H.; Kim, S. J. *Phys. Chem. Chem. Phys.* **2014**, *16*, 103−109.
(195) Hoque, M. A.; Hassan, F. M.; Higgins, D.; Choi, J. Y.; Pritzker, M.; Knights, S.; Ye, S.; Chen, Z. *Adv. Mater.* **2015**, *27*, 1229−1234.
(196) Chen, X.; Chen, X.; Xu, X.; Yang, Z.; Liu, Z.; Zhang, L.; Xu, X.; Chen, Y.; Huang, S. *Nanoscale* **2014**, *6*, 13740−13747.
(197) Chen, L.; Cui, X.; Wang, Y.; Wang, M.; Qiu, R.; Shu, Z.; Zhang, L.; Hua, Z.; Cui, F.; Wei, C.; Shi, J. *Dalton Trans.* **2014**, *43*, 3420−3423.
(198) Zhang, X.; Lu, Z.; Fu, Z.; Tang, Y.; Ma, D.; Yang, Z. *J. Power Sources* **2015**, *276*, 222−229.
(199) Razmjooei, F.; Singh, K. P.; Bae, E. J.; Yu, J.-S. *J. Mater. Chem. A* **2015**, *3*, 11031−11039.
(200) Fei, H. L.; Ye, R. Q.; Ye, G. L.; Gong, Y. J.; Peng, Z. W.; Fan, X. J.; Samuel, E. L. G.; Ajayan, P. M.; Tour, J. M. *ACS Nano* **2014**, *8*, 10837−10843.
(201) Laursen, A. B.; Varela, A. S.; Dionigi, F.; Fanchiu, H.; Miller, C.; Trinhammer, O. L.; Rossmeisl, J.; Dahl, S. *J. Chem. Educ.* **2012**, *89*, 1595−1599.
(202) Trasatti, S. *J. Electroanal. Chem. Interfacial Electrochem.* **1971**, *33*, 351−378.
(203) Durst, J.; Siebel, A.; Simon, C.; Hasche, F.; Herranz, J.; Gasteiger, H. A. *Energy Environ. Sci.* **2014**, *7*, 2255−2260.
(204) Perez, J.; Gonzalez, E. R.; Villullas, H. M. *J. Phys. Chem. B* **1998**, *102*, 10931−10935.
(205) Schmidt, T. J.; Ross, P. N.; Markovic, N. M. *J. Electroanal. Chem.* **2002**, *524*, 252−260.
(206) Smiljanić, M.; Srejić, I.; Grgur, B.; Rakočević, Z.; Štrbac, S. *Electrochim. Acta* **2013**, *88*, 589−596.
(207) Greeley, J.; Nørskov, J. K.; Kibler, L. A.; El-Aziz, A. M.; Kolb, D. M. *ChemPhysChem* **2006**, *7*, 1032−1035.
(208) Jakšić, M. M. *Electrochim. Acta* **1984**, *29*, 1539−1550.
(209) Endoh, E.; Otouma, H.; Morimoto, T.; Oda, Y. *Int. J. Hydrogen Energy* **1987**, *12*, 473−479.
(210) Lasia, A.; Rami, A. *J. Electroanal. Chem. Interfacial Electrochem.* **1990**, *294*, 123−141.
(211) Rami, A.; Lasia, A. *J. Appl. Electrochem.* **1992**, *22*, 376−382.
(212) Le Goff, A.; Artero, V.; Jousselme, B.; Tran, P. D.; Guillet, N.; Metaye, R.; Fihri, A.; Palacin, S.; Fontecave, M. *Science* **2009**, *326*, 1384−1387.
(213) Bhugun, I.; Lexa, D.; Saveant, J. M. *J. Am. Chem. Soc.* **1996**, *118*, 3982−3983.
(214) Torresi, R. M.; Camara, O. R.; Depauli, C. P.; Giordano, M. C. *Electrochim. Acta* **1987**, *32*, 1291−1301.
(215) Boodts, J. C. F.; Trasatti, S. *J. Appl. Electrochem.* **1989**, *19*, 255−262.
(216) Gong, M.; Zhou, W.; Tsai, M. C.; Zhou, J.; Guan, M.; Lin, M. C.; Zhang, B.; Hu, Y.; Wang, D. Y.; Yang, J.; Pennycook, S. J.; Hwang, B. J.; Dai, H. *Nat. Commun.* **2014**, *5*, 4695.
(217) Xu, Y. F.; Gao, M. R.; Zheng, Y. R.; Jiang, J.; Yu, S. H. *Angew. Chem., Int. Ed.* **2013**, *52*, 8546−8550.
(218) Hunt, S. T.; Nimmanwudipong, T.; Roman-Leshkov, Y. *Angew. Chem., Int. Ed.* **2014**, *53*, 5131−5136.
(219) Popczun, E. J.; McKone, J. R.; Read, C. G.; Biacchi, A. J.; Wiltrout, A. M.; Lewis, N. S.; Schaak, R. E. *J. Am. Chem. Soc.* **2013**, *135*, 9267−9270.
(220) Kibsgaard, J.; Jaramillo, T. F. *Angew. Chem., Int. Ed.* **2014**, *53*, 14433−14437.
(221) Xing, Z.; Liu, Q.; Asiri, A. M.; Sun, X. *Adv. Mater.* **2014**, *26*, 5702−5707.
(222) Hinnemann, B.; Moses, P. G.; Bonde, J.; Jorgensen, K. P.; Nielsen, J. H.; Horch, S.; Chorkendorff, I.; Nørskov, J. K. *J. Am. Chem. Soc.* **2005**, *127*, 5308−5309.
(223) Lv, X.-J.; She, G.-W.; Zhou, S.-X.; Li, Y.-M. *RSC Adv.* **2013**, *3*, 21231−21236.

DOI: 10.1021/acscatal.5b00991
ACS Catal. 2015, 5, 5207−5234

(224) Bonde, J.; Moses, P. G.; Jaramillo, T. F.; Nørskov, J. K.; Chorkendorff, I. *Faraday Discuss.* **2009**, *140*, 219−231.
(225) Nicolosi, V.; Chhowalla, M.; Kanatzidis, M. G.; Strano, M. S.; Coleman, J. N. *Science* **2013**, *340*, 1226419.
(226) Coleman, J. N.; Lotya, M.; O'Neill, A.; Bergin, S. D.; King, P. J.; Khan, U.; Young, K.; Gaucher, A.; De, S.; Smith, R. J.; Shvets, I. V.; Arora, S. K.; Stanton, G.; Kim, H. Y.; Lee, K.; Kim, G. T.; Duesberg, G. S.; Hallam, T.; Boland, J. J.; Wang, J. J.; Donegan, J. F.; Grunlan, J. C.; Moriarty, G.; Shmeliov, A.; Nicholls, R. J.; Perkins, J. M.; Grieveson, E. M.; Theuwissen, K.; McComb, D. W.; Nellist, P. D.; Nicolosi, V. *Science* **2011**, *331*, 568−571.
(227) Wang, Q. H.; Kalantar-Zadeh, K.; Kis, A.; Coleman, J. N.; Strano, M. S. *Nat. Nanotechnol.* **2012**, *7*, 699−712.
(228) Xu, M.; Liang, T.; Shi, M.; Chen, H. *Chem. Rev.* **2013**, *113*, 3766−3798.
(229) Lukowski, M. A.; Daniel, A. S.; Meng, F.; Forticaux, A.; Li, L.; Jin, S. *J. Am. Chem. Soc.* **2013**, *135*, 10274−10277.
(230) Yang, J.; Voiry, D.; Ahn, S. J.; Kang, D.; Kim, A. Y.; Chhowalla, M.; Shin, H. S. *Angew. Chem., Int. Ed.* **2013**, *52*, 13751−13754.
(231) Li, Y.; Wang, H.; Xie, L.; Liang, Y.; Hong, G.; Dai, H. *J. Am. Chem. Soc.* **2011**, *133*, 7296−7299.
(232) Kong, D.; Wang, H.; Lu, Z.; Cui, Y. *J. Am. Chem. Soc.* **2014**, *136*, 4897−4900.
(233) Misra, A.; Giri, J.; Daraio, C. *ACS Nano* **2009**, *3*, 3903−3908.
(234) Zhuo, J.; Wang, T.; Zhang, G.; Liu, L.; Gan, L.; Li, M. *Angew. Chem., Int. Ed.* **2013**, *52*, 10867−10870.
(235) Zhao, Y.; Zhao, F.; Wang, X.; Xu, C.; Zhang, Z.; Shi, G.; Qu, L. *Angew. Chem., Int. Ed.* **2014**, *53*, 13934−13939.
(236) Duan, H.; Yan, N.; Yu, R.; Chang, C. R.; Zhou, G.; Hu, H. S.; Rong, H.; Niu, Z.; Mao, J.; Asakura, H.; Tanaka, T.; Dyson, P. J.; Li, J.; Li, Y. D. *Nat. Commun.* **2014**, *5*, 3093.
(237) Zou, X.; Huang, X.; Goswami, A.; Silva, R.; Sathe, B. R.; Mikmekova, E.; Asefa, T. *Angew. Chem., Int. Ed.* **2014**, *53*, 4372−4376.
(238) Liu, Y.; Yu, H.; Quan, X.; Chen, S.; Zhao, H.; Zhang, Y. *Sci. Rep.* **2014**, *4*, 6843.
(239) Sathe, B. R.; Zou, X.; Asefa, T. *Catal. Sci. Technol.* **2014**, *4*, 2023−2030.
(240) Zheng, Y.; Jiao, Y.; Zhu, Y.; Li, L. H.; Han, Y.; Chen, Y.; Du, A.; Jaroniec, M.; Qiao, S. Z. *Nat. Commun.* **2014**, *5*, 3783.
(241) Chen, S.; Duan, J.; Tang, Y. H.; Jin, B.; Qiao, S. Z. *Nano Energy* **2015**, *11*, 11−18.
(242) Hou, Y.; Wen, Z.; Cui, S.; Ci, S.; Mao, S.; Chen, J. *Adv. Funct. Mater.* **2015**, *25*, 872−882.
(243) Zheng, Y.; Jiao, Y.; Li, L. H.; Xing, T.; Chen, Y.; Jaroniec, M.; Qiao, S. Z. *ACS Nano* **2014**, *8*, 5290−5296.
(244) Dau, H.; Zaharieva, I. *Acc. Chem. Res.* **2009**, *42*, 1861−1870.
(245) McCrory, C. C.; Jung, S.; Peters, J. C.; Jaramillo, T. F. *J. Am. Chem. Soc.* **2013**, *135*, 16977−16987.
(246) Parsons, R. *Trans. Faraday Soc.* **1958**, *54*, 1053−1063.
(247) Man, I. C.; Su, H.-Y.; Calle-Vallejo, F.; Hansen, H. A.; Martínez, J. I.; Inoglu, N. G.; Kitchin, J.; Jaramillo, T. F.; Nørskov, J. K.; Rossmeisl, J. *ChemCatChem* **2011**, *3*, 1159−1165.
(248) Damjanovic, A.; Dey, A.; Bockris, J. O. M. *J. Electrochem. Soc.* **1966**, *113*, 739−746.
(249) Subbaraman, R.; Tripkovic, D.; Chang, K. C.; Strmcnik, D.; Paulikas, A. P.; Hirunsit, P.; Chan, M.; Greeley, J.; Stamenkovic, V.; Markovic, N. M. *Nat. Mater.* **2012**, *11*, 550−557.
(250) Takashima, T.; Hashimoto, K.; Nakamura, R. *J. Am. Chem. Soc.* **2012**, *134*, 18153−18156.
(251) Indra, A.; Menezes, P. W.; Zaharieva, I.; Baktash, E.; Pfrommer, J.; Schwarze, M.; Dau, H.; Driess, M. *Angew. Chem., Int. Ed.* **2013**, *52*, 13206−13210.
(252) Smith, R. D.; Prevot, M. S.; Fagan, R. D.; Zhang, Z.; Sedach, P. A.; Siu, M. K.; Trudel, S.; Berlinguette, C. P. *Science* **2013**, *340*, 60−63.
(253) Risch, M.; Stoerzinger, K. A.; Maruyama, S.; Hong, W. T.; Takeuchi, I.; Shao-Horn, Y. *J. Am. Chem. Soc.* **2014**, *136*, 5229−5232.
(254) Maiyalagan, T.; Jarvis, K. A.; Therese, S.; Ferreira, P. J.; Manthiram, A. *Nat. Commun.* **2014**, *5*, 3949.
(255) Hunter, B. M.; Blakemore, J. D.; Deimund, M.; Gray, H. B.; Winkler, J. R.; Müller, A. M. *J. Am. Chem. Soc.* **2014**, *136*, 13118−13121.
(256) Song, F.; Hu, X. *Nat. Commun.* **2014**, *5*, 4477.
(257) Lu, X.; Yim, W. L.; Suryanto, B. H.; Zhao, C. *J. Am. Chem. Soc.* **2015**, *137*, 2901−2907.
(258) Ma, T. Y.; Dai, S.; Jaroniec, M.; Qiao, S. Z. *Angew. Chem., Int. Ed.* **2014**, *53*, 7281−7285.
(259) Zhang, J.; Zhao, Z.; Xia, Z.; Dai, L. *Nat. Nanotechnol.* **2015**, *10*, 444−452.
(260) Chen, S.; Duan, J. J.; Ran, J.; Jaroniec, M.; Qiao, S. Z. *Energy Environ. Sci.* **2013**, *6*, 3693−3699.
(261) Wang, J.; Wang, K.; Wang, F. B.; Xia, X. H. *Nat. Commun.* **2014**, *5*, 5285.
(262) Singh, S. K.; Dhavale, V. M.; Kurungot, S. *ACS Appl. Mater. Interfaces* **2015**, *7*, 442−451.
(263) Chen, S.; Duan, J. J.; Jaroniec, M.; Qiao, S. Z. *Angew. Chem., Int. Ed.* **2013**, *52*, 13567−13570.
(264) Chen, S.; Duan, J. J.; Jaroniec, M.; Qiao, S. Z. *Adv. Mater.* **2014**, *26*, 2925−2930.
(265) Chen, S.; Duan, J.; Ran, J.; Qiao, S. Z. *Adv. Sci.* **2015**, *2*, 1400015.

DOI: 10.1021/acscatal.5b00991
ACS Catal. 2015, 5, 5207−5234